Signal Sources and Sensors

Authors:

Ajay K. Poddar (1), Ulrich L. Rohde (1, 2,),

Author affiliations:

(1) Synergy Microwave, NJ, USA

(2) Massachusetts Institute of Technology, MIT, Microsystems Technology Laboratories, USA

Introduction

Metamaterial Möbius-Strips (MMS) has captured the interest of research scientists because of distinctive properties, such as topological symmetry (property, conserved when the system undergoes an alteration (deformation, twisting and stretching of objects) and negative index ($n = -\sqrt{\epsilon\mu}$; $\varepsilon < 0$, $\mu < 0$) characteristics. Figure (1) shows the typical negative index ($\varepsilon < 0$, $\mu < 0$) Möbius-Strips formed Grapheme nano-ribbons, which possess topology-induced desirable high Q- factor components and desirable electromagnetic properties. Unlike conventional materials, which interact with EM (electromagnetic) wave based on their chemical composition, the properties of NIM (negative index material), and known as metamaterial come from their geometric topology structure.

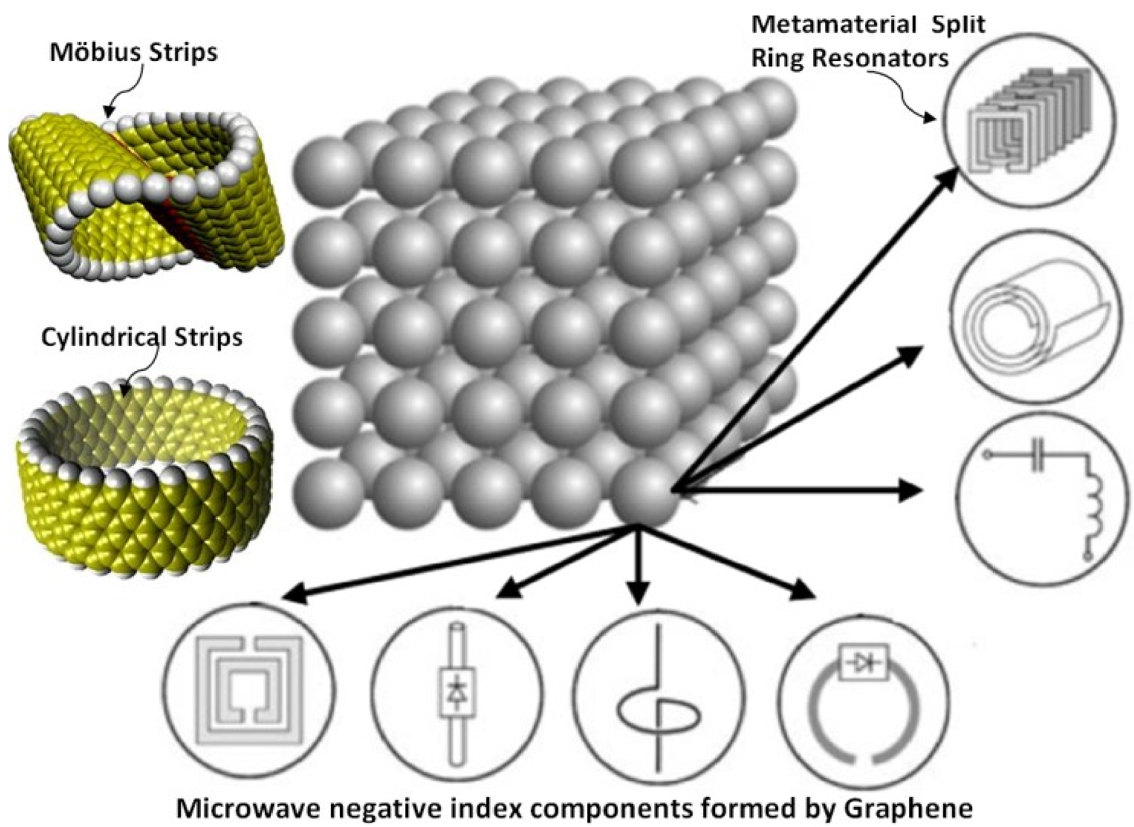

Fig.1: Möbius-Strips structure formed by Grapheme nanoribbons exhibits negative index properties ($\varepsilon<0$, $\mu<0$), well suited suitable for high quality factor microwave frequency components

NIMs (Negative Index Materials) are artificial engineered topological structures illustrated in Figure (1), intended to modify the bulk permeability and permittivity of the medium, which can be realized by placing periodically unit cell NIM's structures under the constraints of their size (typically less than the wavelength of incident EM wave). It is interesting to note that by changing the position, orientation, excitation of NIM's structure, important parameters (permittivity, permeability, refractive index, transmission, reflection, impedance, and coupling) can be tuned and optimized for desired applications. There are many ways to vary the properties of NIM, such as by using ferrites, liquid crystals, frequency-selective surfaces, and hybrid-NIM or by manipulating the lattice structure.

Figure (2) shows the typical characteristics of the medium that explains the properties of natural and artificial engineered composite material [1]. As shown in Figure (2), the third quadrant describes the properties of left-handed medium that posses NIM (negative index material: $n = -\sqrt{\epsilon\mu}$; ε <0, μ <0) characteristics. The evanescent-mode energy storing and resonant characteristics of the third-quadrant material enables potential applications in electronics, medical, space, and optics. Hence, it is important to understand the fundamental EM dynamics of the third-quadrant material (ε < 0, μ < 0) for designing NIMS resonator based electronic signal sources. It is important to note that exact characterization of ε and μ of NIM structure is challenging task for wideband frequency operation.

While it is possible to characterize the NIM's in terms of refractive index (*n)* and normalized impedance (*z*) but these do not provide meaningful information. The ongoing effort by research scientists is to categorize NIM-structure by effective constitutive parameters: $\varepsilon_r = n/z$, $\mu_r = n \times z$, which gives a direct and an understandable interpretation of NIM based element.

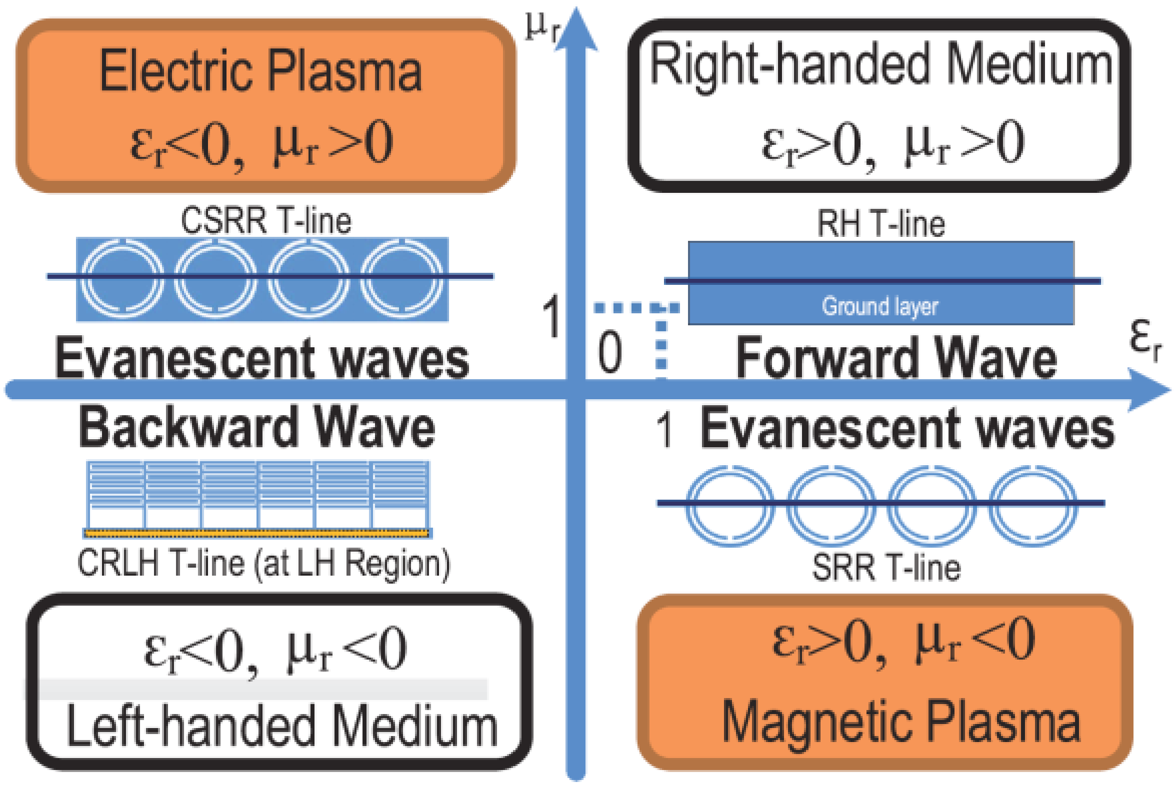

Fig. 2: A typical representation of the medium: 3rd quadrant explains left-handed medium, NIM (negative index) material properties

In addition to this, the justification of using effective constitutive parameters (ε < 0, μ < 0) provide a convenient means to understand the behavior of the artificial engineered NIMs structures without considering in details about the local EM-field distribution. To establish the faithful values of these effective constitutive parameters, numerous methods reported, but none of them provides exact solutions because of the hypothesis of NIM's tiny size and neglecting the couplings. The general isotropic medium model assumes that the induced electric and magnetic dipoles are mutually independent, but in reality this is not always the case. NIMs are intrinsically anisotropic and sometime bianisotropic because of geometry and orientations of their structure. For example, SRs as shown in Figure (3), typically used in NIMs, exhibit simultaneous electric and magnetic response, i.e., corresponding dipoles are coupled [5]. This leads to cross-coupling between electric and magnetic field in SR inspired NIM structures. Therefore, it is not recommended to discount the magneto-electric coupling that depends on shape of inclusions, wave-polarizations, excitation, and orientation of NIM's structures. To account for both asymmetric reflection and magneto-electrical coupling, bianisotropic medium model can be used.

Figure (3) shows the typical circular and square split ring structures for the realization of NIM (negative index material), the size of SRs (split rings) and the distances between them are kept smaller than the wavelength (λ). Under this assumption, SR-NIM structure may present bulk properties and can be characterized by a macroscopic model, with effective index parameter (ε and μ). The expression for index (*n*) is given by

$$n = \pm\sqrt{(\pm\epsilon)(\pm\mu)} = \pm\sqrt{\mu\epsilon} \qquad (1)$$

From (1), the positive sign is used for *n* when ε, μ > 0, whereas the negative sign is used when ε, μ < 0. The assumption of positive index (*n* > 0) implies that the index *n* is a scalar, and does not depend on frequency. But in reality, this is not always true. The energy of the field (*W)* would be negative ($W=\varepsilon E^2+\mu H^2$) value when ε and μ are negative, and this is not possible, hence ε and μ bound to depend on frequency and fall into complex domain [2]. The unified expression of energy *W* can be described by

$$W = \frac{\partial(\omega\varepsilon)}{\partial\omega}E^2 + \frac{\partial(\omega\mu)}{\partial\omega}H^2 \qquad (2)$$

where $\varepsilon(\omega) = \varepsilon'(\omega) + j\varepsilon''(\omega)$ and $\mu(\omega) = \mu'(\omega) + j\mu''(\omega)$

From (2), the electrodynamics of negative index materials (n<0; ε < 0 and μ < 0) would give positive value of *W* for a very broad class of dispersive material characterized by $\varepsilon(\omega)$ and$\mu(\omega)$, exhibit dependency on frequency.

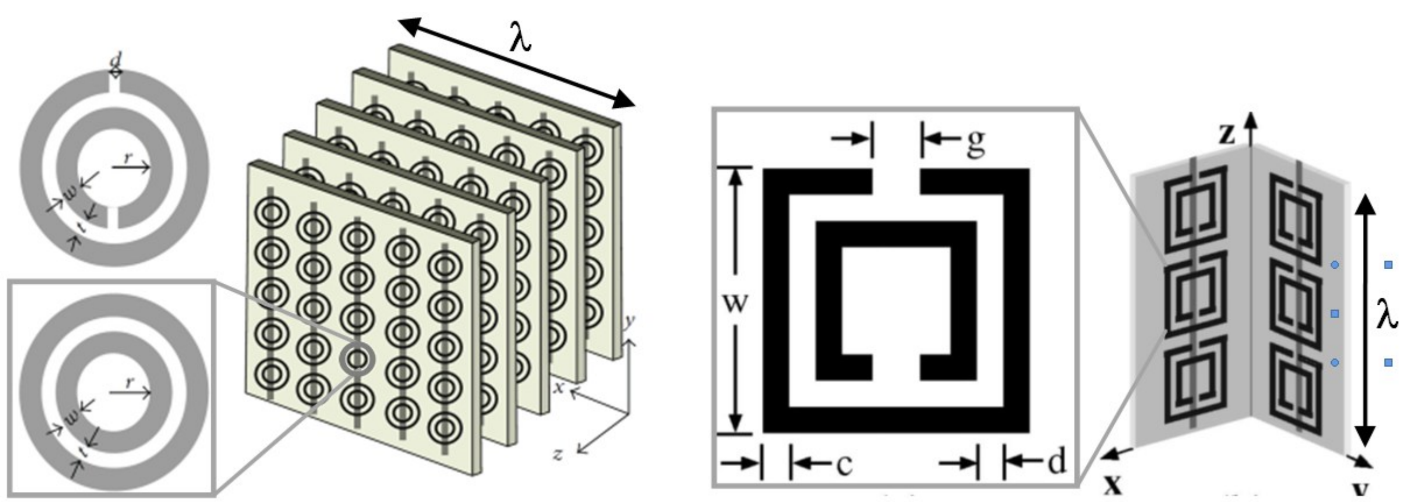

(a) Circular Split Rings

(b) Rectangular Split Ring

Fig. 3: Shows the typical SRRs and the construction of NIM with closed SRR wire structure: (a) Circular Split Ring, and (b) Rectangular Split Ring

○

Any material supporting single propagating mode at a known frequency, usually exhibits well-defined index (*n*), despite the material is homogeneous/continuous or not. But it is not easy to assign normalized impedance (*z*) to a non-homogeneous material, because *z* strongly depends on surface termination and overall size of the material [1]. The classical homogenization theories are typically valid when the unit-cell size is insignificant with respect to the wavelength (the zero frequency limits) and thus might be expected to result in a poor description of negative index materials. The key supposition is, if the wavelength of the incident wave is much larger than the size and spacing between the NIM's unit cell element then it is possible to perform homogenization, and to obtain a approved value of *z* within an acceptable limit of errors [2]-[3].

Assuming the size of NIM's structure is much smaller than $\lambda/10$, homogenization theory can be applied to topology inspired Möbius Strips structure, averaging of Maxwell's equations over small volumes (with respect to wavelength) can be performed to get analogous uniform continuous harmonized medium, described by effective constitutive parameters (ε and μ). It is possible to retrieve values for the complex refractive index (*n*) and wave impedance (*z*) of inhomogeneous periodic NIMS structure, by prior information about termination of the NIMS-unit cell structure, phases and amplitudes of the waves transmitted/reflected from the NIMS sample. But the challenge is if the NIMS structures are not symmetric along the wave propagation direction, 2-different values of impedance (*z*) are retrieved corresponding to 2-incident directions of propagation. This ambiguity in the computation of impedance (*z*) leads to a fundamental ambiguity in the definitions of ε and μ for MIMS, which increases as the ratio of NIMS unit cell dimension to wavelength increases.

The simplest approach of theoretical formulation of SR inspired NIM (negative index material) can be deduced from equivalent circuit model that gives insight into the relationship between the physical properties and geometrical parameters of SRRs as shown in Figures (3) and (4). The analytical values of constitutive parameters (ε_{zz}, μ_{yy}, ξ_0) is given by [5, 13, 17]

$$\varepsilon_z = 1 + \frac{1}{\varepsilon_0 a^3}\left\{\varepsilon_0 \frac{16}{3} r_{ext}^3 + 4 d_{eff}^2 r_0^2 C_{pul}^2 L\left(\frac{\omega^2}{\omega_0^2-\omega^2-i\omega\gamma}\right)\right\} \quad (3)$$

$$\mu_y = 1 + \frac{\mu_0}{a^3}\left\{\frac{\pi^2 r_0}{L}\left(\frac{\omega^2}{\omega_0^2-\omega^2-i\omega\gamma}\right)\right\} \quad (4)$$

$$\xi_0 = -i\sqrt{\frac{\mu_0}{\varepsilon_0 a^3}}\left\{-2i r_0^3 d_{eff} C_{pull}\frac{\omega_0^2}{\omega}\left(\frac{\omega^2}{\omega_0^2-\omega^2-i\omega\gamma}\right)\right\} \quad (5)$$

where $d_{eff} = c + s$, $\gamma = \frac{R}{L}$, $r_0 = r + c + s/2$ and $r_{ext} = r + 2c + s$; L and C_{pull} are the total inductance of the SRR and the capacitance between the rings respectively. From the equivalent circuit model, RR behaves as a resonant *LC* circuit, and that the frequency of the resonance is given by

$$\omega_0^2 = \frac{1}{\left(\frac{1}{2}\pi r_0 C_{pull} + C_{gap}\right)L} \quad (6)$$

L and C_{pull} can be calculated from the analytical equations reported in [17]. C_{gap} is the capacitance of the gap, if the gap is narrow, its capacitance can be analytically written as [18]

$$C_{gap} = \frac{\varepsilon_0 ch}{g} + C_0 \text{ with } C_0 = \varepsilon_0(h + c + g) \quad (7)$$

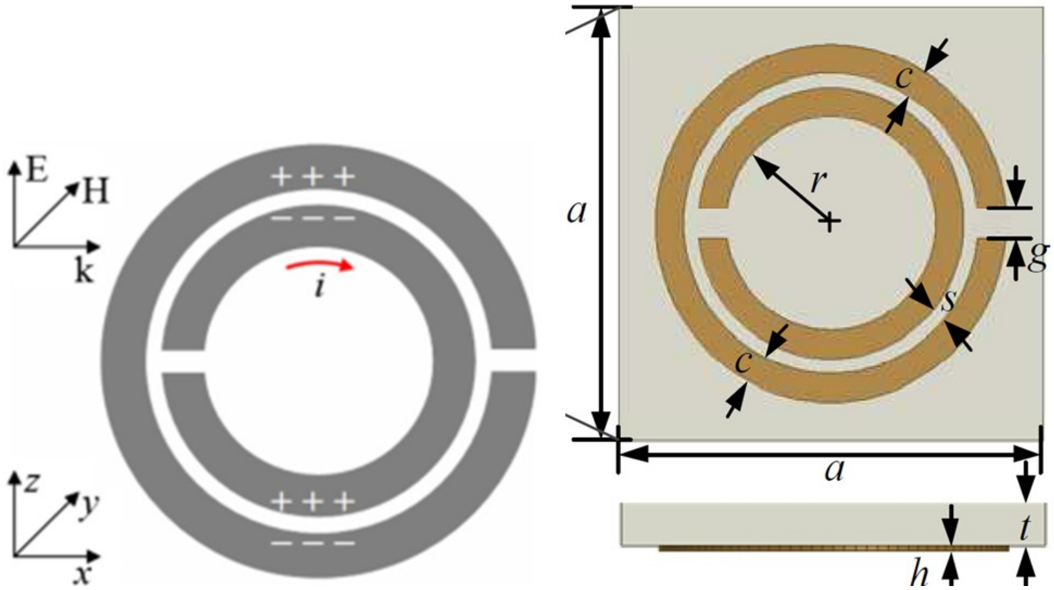

Fig. 4: A typical SRR unit cell shows the asymmetric rings (inner and outer)

From [17], L = 3:9287× 10^{-9} H, C_{pul} = 1:6806 × 10^{-11} F, C_{gap} = 4:1557 × 10^{-15}F and R = 0:4901 Ω at the frequency of resonance. The poor accuracy of analytical method for constitutive parameter calculation given in Equations (3)-(7) and the deficiency for complex models for thicker structures limit its validation. The alternative approach is retrieval technique based on extraction of S-parameters. The advantages of retrieval method are it can be used for simulated and measured *S*-parameter data; thin samples (in the propagation direction) are preferred to minimize the errors.

In general there are 3-methods used for the determination of effective constitutive parameters based on applications and acceptable limit of errors [3]. The first method is to numerically calculate the ratios of the EM (electromagnetic) field inside NIM's structure but this approach is good for numerical simulations, and not appropriate for experimental measurement [4]. The second method calculates the effective constitutive parameters by using analytical models of NIM's structures including numerical averaging of fields. But this technique is not suitable for complex NIM's structures such as NIMS [5]. The third method is a retrieval technique based on the inversion of scattering data (S-parameters) of a finite slab, called the NRW procedure [6]-[7]. NRW (Nicolson–Ross–Weir) method was developed for the measurements of complex permittivity and permeability of natural materials and recently applied to NIMs [1]-[20]. The problem with NRW method arises in case when topology driven NIM's structure undergo asymmetric reflections. Smith *et al.* [2] reported a modified approach to resolve this issue of asymmetric reflections by using averaged value of reflection coefficients. The isotropic medium model cannot duplicate this property, as it is intrinsically symmetric, hence it is important to understand the EM dynamics of SR inspired NIM media, which inherently possess reflection asymmetric structures ($S_{11} \neq S_{22}$) [21].

I. EM Dynamics of Media

The fundamental equations describing characteristics of EM waves in a biaxial anisotropic medium (or simply called biaxial) are complex than the isotropic equations. Isotropic materials have a single permittivity ε. In an isotropic media, the constitutive relations that relate the electric flux density $\overline{D}$ to the electric field intensity $\overline{E}$ and the magnetic flux density $\overline{B}$ to the magnetic field intensity $\overline{H}$ are given by

$$\overline{D} = \varepsilon\overline{E} = \varepsilon_o\varepsilon_r\overline{E} \; ; \overline{B} = \mu\overline{H} = \mu_0\mu_r\overline{H} \qquad (8)$$

From (8), the permittivity of the medium (ε) describes the medium's electrical properties and the permeability (μ) describes its magnetic properties. The time-harmonic forms of Maxwell's equations for isotropic media are given by

$$\nabla \times \bar{E} = -i\omega\mu\bar{H} \qquad (9)$$

$$\nabla \times \bar{H} = i\omega\varepsilon\bar{E} + \bar{J} \qquad (10)$$

$$\nabla . \bar{D} = \rho_V \qquad (11)$$

$$\nabla . \bar{B} = 0 \qquad (12)$$

A medium is called electrically anisotropic if $\bar{D} = \overline{\bar{\varepsilon} \cdot} \bar{E}$, where $\bar{\bar{\varepsilon}}$ is the permittivity tensor. A medium is magnetically anisotropic if $\bar{B} = \bar{\bar{\mu}} \cdot \bar{H}$, where $\bar{\bar{\mu}}$ is the permeability tensor, note that $\bar{B}$ and $\bar{H}$ are no longer parallel. A medium can be both electrically and magnetically anisotropic.

In electrically anisotropic case $\bar{D}$ and $\bar{E}$ are no longer parallel, $\bar{\bar{\varepsilon}}$ is given by

$$\bar{\bar{\varepsilon}} = \begin{pmatrix} \varepsilon_{xx} & \varepsilon_{xy} & \varepsilon_{xz} \\ \varepsilon_{yx} & \varepsilon_{yy} & \varepsilon_{yz} \\ \varepsilon_{zx} & \varepsilon_{zy} & \varepsilon_{zz} \end{pmatrix} \qquad (13)$$

For example, crystals, in general, are described by a symmetric permittivity tensor; there always exist a coordinate transformation that transforms the symmetric matrix $\bar{\bar{\varepsilon}}$ to a diagonal matrix as given by

$$\bar{\bar{\varepsilon}} = \begin{pmatrix} \varepsilon_{xx} & 0 & 0 \\ 0 & \varepsilon_{yy} & 0 \\ 0 & 0 & \varepsilon_{zz} \end{pmatrix} \qquad (14)$$

From (14), new coordinate system is called the principal system, and the three coordinate axes are called the principal axes. For cubic crystal $\varepsilon_{xx} = \varepsilon_{yy} = \varepsilon_{zz} = \varepsilon$, the crystal is isotropic.

$$\bar{\bar{\varepsilon}} = \begin{pmatrix} \varepsilon & 0 & 0 \\ 0 & \varepsilon & 0 \\ 0 & 0 & \varepsilon \end{pmatrix} \qquad (15)$$

For tetragonal, hexagonal, and rhombohedra crystals two of the three ε are equal, such crystal is called uniaxial.

Uniaxial anisotropic materials have two different permittivity values. Uniaxial materials have the same permittivity along two dimensions and a different permittivity along the third dimension. The axis along the direction of the unique permittivity value is called the optic axis. An unrotated uniaxial permittivity tensor can be written as

$$\bar{\bar{\varepsilon}} = \begin{pmatrix} \varepsilon & 0 & 0 \\ 0 & \varepsilon & 0 \\ 0 & 0 & \varepsilon_{zz} \end{pmatrix} \qquad (16)$$

From (16), the principal axis that is different (exhibits anisotropy) is called the optical axis (*z*-axis is the optical axis), there exists a two dimensional degeneracy. If $\varepsilon_{zz} > \varepsilon$, the medium exhibits positive uniaxial behavior, and if $\varepsilon_{zz} > \varepsilon$, the medium shows negative uniaxial characteristics.

If $\varepsilon_{xx} \neq \varepsilon_{yy} \neq \varepsilon_{zz}$, the crystal is biaxial, examples of biaxial crystals are orthorhombic, monoclinic, and triclinic. The defining property of electrically biaxial media is the permittivity tensor $\bar{\bar{\varepsilon}}$.

If the medium is biaxial anisotropic, the permittivity and permeability of medium take on a tensor form. From (8), the set of matrix equations can be described by

$$\overline{D} = \bar{\bar{\varepsilon}} \cdot \overline{E} = \varepsilon_o \bar{\bar{\varepsilon_r}} \cdot \overline{E}\ ; \overline{B} = \bar{\bar{\mu}} \cdot \overline{H} = \mu_0 \bar{\bar{\mu}}_r \overline{\cdot H} \qquad (17)$$

where$\bar{\bar{\varepsilon_r}}$ and $\bar{\bar{\mu}}_r$ are relative permittivity and permeability tensors, respectively. From (17), the change in constitutive relations will also affect Maxwell's equations (9)-(12) in the medium, is given by

$$\nabla \times \overline{E} = -i\omega\bar{\bar{\mu}}\overline{H} \qquad (18)$$

$$\nabla \times \overline{H} = i\omega\bar{\bar{\varepsilon}}\overline{E} + \overline{J} \qquad (19)$$

$$\nabla . \overline{D} = \rho_V \qquad (20)$$

$$\nabla . \overline{B} = 0 \qquad (21)$$

The NIMs exhibit bianisotropic medium, provide coupling between electric and magnetic fields. The constitutive relations for a bianisotropic medium is given by

$$\vec{D} = \bar{\bar{\varepsilon}} . \vec{E} + \bar{\bar{\xi}} . \vec{H} \qquad (22)$$

$$\vec{B} = \bar{\bar{\mu}} . \vec{H} + \bar{\bar{\xi}} . \vec{E} \qquad (23)$$

A bianisotropic medium placed in an electric or magnetic field becomes both polarized and magnetized. Almost any media in motion becomes bianisotropic. The first cases of bianisotropic materials were indeed moving dielectrics and magnetic materials in the presence of electric or magnetic fields. The topics of moving NIMs and their constitutive relations are the subject of the relativistic electromagnetic theory, can lead to Casmir effect (anti-gravity) [15]. The permittivity described in (16), represents an unrotated uniaxial medium with optic axis along the z-direction. Biaxially anisotropic materials have three unique values in the permittivity tensor and they have two optic axes. An unrotated biaxial permittivity tensor, given by

$$\bar{\bar{\varepsilon}} = \begin{pmatrix} \varepsilon_x & 0 & 0 \\ 0 & \varepsilon_y & 0 \\ 0 & 0 & \varepsilon_z \end{pmatrix} \qquad (24)$$

where $\varepsilon_x \neq \varepsilon_y \neq \varepsilon_z$. From (8), principal axes of a biaxial medium are aligned with the Cartesian coordinate system.

For better understanding, Figure (5) shows the plots of the unrotated biaxial medium; the inner surface called as "a-wave vector surface" and the outer surface is the "b-wave vector surface". The intersecting line is one of the optic axes, it can be seen from Figure (5) that the optic axis intersects the wave vector surfaces at some point and the "b-wave wave vector surface" is at a local minimum at the point of intersection [10]. If, the biaxial medium is arbitrarily oriented with respect to the coordinate system, the permittivity tensor representation would be in complex and not as simple described in (8).

The evaluation of the tensor for an arbitrarily oriented biaxial medium is given by applying rotations to the tensor in (8), the wave vector surfaces are shown in Figure (6). Studying the wave vector surfaces of the unbounded region as shown in Figures (5) and (6) give insight into how the wave influences the important parameters (ε, μ, n, z) in the composite NIM structures, which are intrinsically anisotropic and sometime bianisotropic for NIMS structure because of geometry and orientations of their structure.

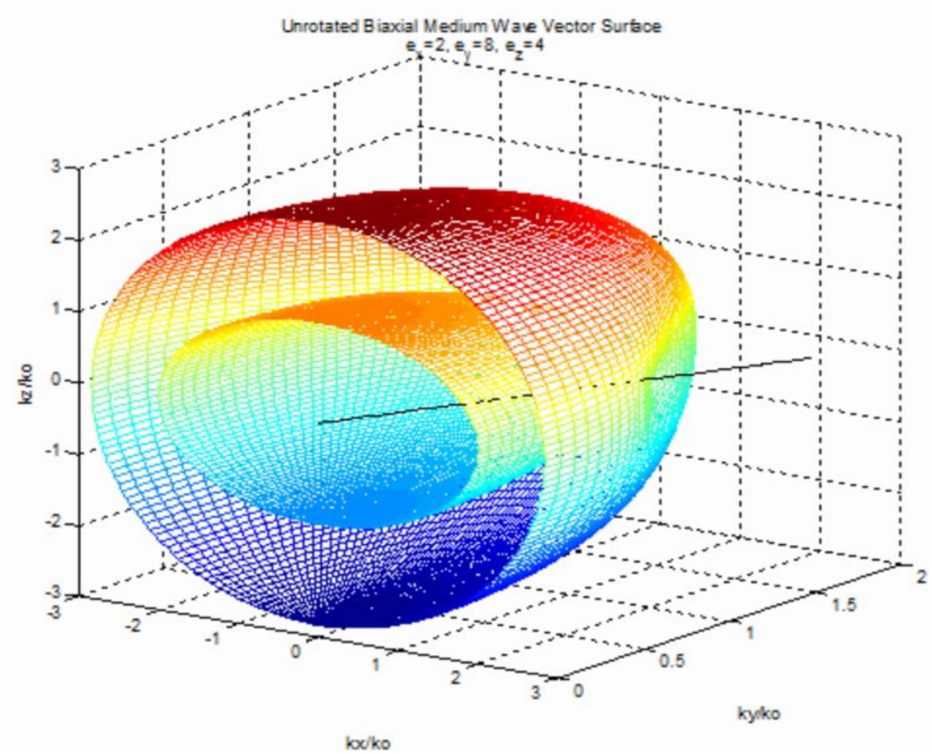

Fig. 5: Wave vector surface: unrotated biaxial medium (ε_x, ε_y, ε_z) = (2, 8, 4), plotted over: $0 \leq \theta \leq \pi$, $0 \leq \varphi \leq \pi$

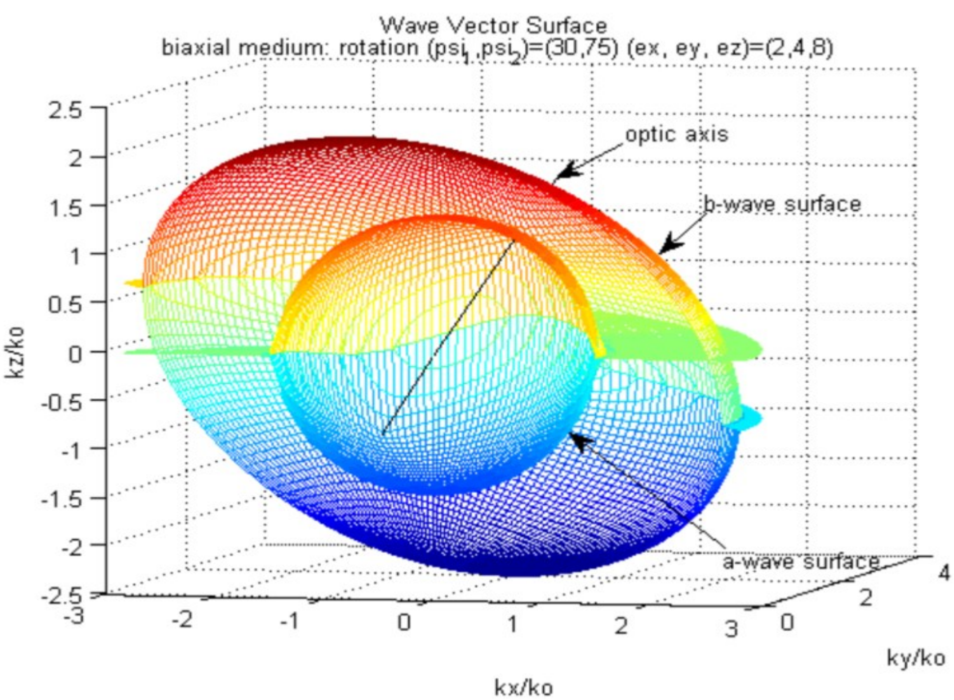

Fig.6: Wave vector surface: rotated biaxial medium (ε_x, ε_y, ε_z) = (2, 8, 4), rotated by (ψ_1 ψ_2) = (30˚, 75˚)

II. Constitutive Effective Papameters

Most of the NIMs presented over the past several years are artificially engineered SR-inspired periodic structures [1]-[25]. It is convenient to extract the parameters from a unit cell of periodic structures through numerical approaches. It has been demonstrated that under the condition of long wavelength the materials with periodic structures can be viewed as a homogeneous medium and their properties can be described by the effective medium parameters. The properties of a periodic structure can be determined from the transfer-matrix (T) which associated with the fields of a unit cell.

NIM structures fall into the category of anisotropic and bianisotropic (cross-coupling exists between electric and magnetic fields in bianisotropic) due to their orientation and special geometry structures. When computing the effective parameters of NIM structures, magneto-electric coupling is a critical parameter. The simplified approach to retrieve the coupling parameter of a bianisotropic material from *S*-parameters is based on transfer-matrix method. The transfer-matrix method has been used to retrieve the effective EM (electromagnetic) parameters of a homogeneous and non-homogeneous material [1]-[2].

Figure (7) shows a typical of bianisotropic slab of thickness'', placed in air, illustrates the direction of S (Scattering) parameters. For a material consisting of periodic structures, there exists a phase advance per unit cell, which can be defined by the periodicity [13].

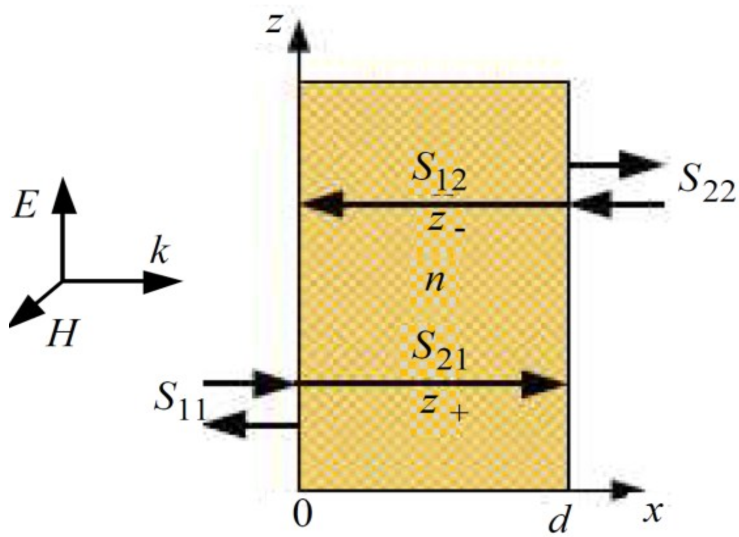

Fig.7. Plane wave incident in the *x* direction into a bianisotropic [13]

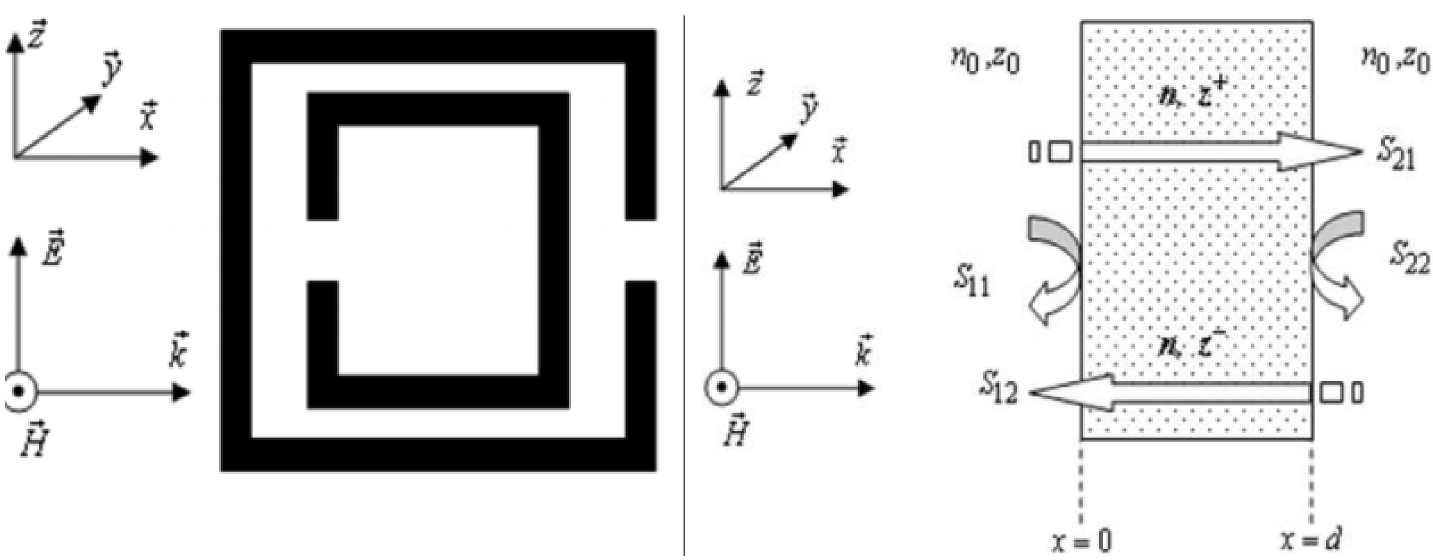

Fig. 8. (a) Structure of the planar SRR and (b) a homogeneous bianisotropic material slab with thickness *d* suspended in air and *S*-parameters used in the determination of the forward and backward wave impedances [3].

Chen et al. [16] extracted effective constitutive parameters of bianisotropic negative index material from *S*-parameters for various wave polarizations using numerical approach for a plane wave polarized in the *z* direction and incident in the *x* direction. Figure (8) shows the triplet $[\overline{k_x}, -H_y, E_z]$based on right-handed coordinate system, containing electric and magnetic field.

As shown in Figure (8), the plane wave polarized in z- axis propagates along the *x*- direction, the electric fields in the *z*-direction will induce magnetic dipoles and the magnetic fields in the *y*- direction will induce electric dipoles due to the asymmetry of the inner and outer rings. It means that electric dipoles cannot only be excited by the E-fields but also by the H-fields. Similarly, magnetic dipoles cannot only be excited by the magnetic (H) fields but also by the electric fields (H).

Assuming that medium is reciprocal and that the harmonic time dependence is $e^{-i\omega t}$, constitutive relationship is given 19]

$$\vec{D} = \bar{\bar{\varepsilon}}.\vec{E} + \bar{\bar{\xi}}.\vec{H} \qquad (25)$$

$$\vec{B} = \bar{\bar{\mu}}.\vec{H} + \bar{\bar{\xi}}.\vec{E} \qquad (26)$$

$$\bar{\bar{\varepsilon}} = \varepsilon_0 \begin{pmatrix} \varepsilon_{xx} & 0 & 0 \\ 0 & \varepsilon_{yy} & 0 \\ 0 & 0 & \varepsilon_{zz} \end{pmatrix}, \quad \bar{\bar{\mu}} = \mu_0 \begin{pmatrix} \mu_{xx} & 0 & 0 \\ 0 & \mu_{yy} & 0 \\ 0 & 0 & \mu_{zz} \end{pmatrix} \quad (27)$$

$$\bar{\bar{\xi}} = \frac{1}{c} \begin{pmatrix} 0 & 0 & 0 \\ 0 & 0 & 0 \\ 0 & -i\xi_0 & 0 \end{pmatrix}, \quad \bar{\bar{\zeta}} = \frac{1}{c} \begin{pmatrix} 0 & 0 & 0 \\ 0 & 0 & i\xi_0 \\ 0 & 0 & 0 \end{pmatrix} \quad (28)$$

where $\vec{E}$, $\vec{H}$, and $\vec{D}$, are electric field, magnetic field intensities, and flux densities; $\varepsilon_0$and μ_0 are the permittivity and permeability of the vacuum; *c* is the speed of light in vacuum; and other four quantities are dimensionless and are unknowns. When a plane wave polarized in the *z*-direction incident in the *x*-direction, only 2-components of EM-fields (E_z and H_y) and 3-EM parameters (ε_{zz}, μ_{yy}, ξ_0) are included.

The numerical formulation is done for the determination of the forward and backward wave impedances entailed by parameters ε_{zz}, μ_{yy} and ξ_0, since other unknown four quantities ε_{xx} , ε_{yy} , μ_{xx} , and μ_{zz} are not related to the bianisotropic structure in Figure 8(b).

From (18)-(19):

$$\frac{\partial^2 E_z}{\partial x^2} + k_x^2 E_z = 0, \quad \frac{\partial^2 H_y}{\partial x^2} + k_x^2 H_y = 0 \quad (29)$$

$$Z^+ = \frac{E^+}{H^+} = Z_0 \frac{\mu_{yy}}{(n + i\xi_0)} \quad (30)$$

$$Z^{-} = \frac{E^{-}}{H^{-}} = Z_0 \frac{\mu_{yy}}{(n-i\xi_0)}, Z_0 = \sqrt{\frac{\mu_0}{\varepsilon_0}} \qquad (31)$$

$$z^{\pm} = \frac{Z^{\pm}}{Z_0}; \;\; z^{+} = \frac{Z^{+}}{Z_0}; \;\; z^{+} = \frac{Z^{+}}{Z_0} \quad (32)$$

$$k_x^2 = k_0^2\left(\varepsilon_{zz}\mu_{yy} - \xi_0^2\right), \; k_x = nk_0 \qquad (33)$$

$$n^2 = \varepsilon_{zz}\mu_{yy} - \xi_0^2 \;, \; n = \pm\sqrt{\varepsilon_{zz}\mu_{yy} - \xi_0^2} \qquad (34)$$

where E_z and H_y are the *z* and *y* components of $\vec{E}$ and $\vec{H}$; k_x and k_0 are the wave number of the wave propagating in the *x* direction and in free-space, Z^{+} and Z^{-} are wave impedances inside the medium for forward $(+\hat{x})$ and backward $(-\hat{x})$ propagations; z^{+} and z^{-} are normalized (or non-dimensionalized) wave impedances in respective directions; Z_0 is the wave impedance (or intrinsic impedance) in air; and *n* is the refractive index of the negative index structure.

From (30)-(31), bianisotropic NIM (negative index material) structure samples exhibit different values of wave- impedances for forward and backward wave propagating direction [2, 20]. The non-homogeneous periodic NIM structure does not exhibits distinct impedance values because ratio of $E/\overline{H}'$ will vary periodically throughout the structure. This variation is negligible if the NIM structure unit cell sizes are small relative to the wavelength. The important point to note here, the lack of a unique definition for $z^{\pm}$ indicates that the values of ε and μ retrieved are not assignable but they can be applied if the NIM formed by periodic structure terminated always in the same location of the unit cell. The surface termination has an increasing influence on the scattering properties of the structure as the scale of inhomogeneity increases relative to the wavelength.

It has been demonstrated that under the condition of long wavelength the materials with periodic structures can be viewed as a homogeneous medium and their properties can be described by the effective medium parameters. The properties of a periodic structure can be determined from the transfer-matrix (T) which associated with the fields of a unit cell. We express the fields in the form of a vector F =$\overline{F} = (\overline{E}, \overline{H}')^T$, where $\overline{E}$ and $\overline{H}$ are the complex amplitudes of the electric and magnetic fields located on the left-hand and right-hand faces of a slab. The magnetic field is a reduced field with the normalization form $\overline{H}' = i\omega\mu\overline{H}$. The relations of fields on two sides of a slab can be expressed as

$$\overline{F}(x+d) = e^{i\alpha d}\overline{F}(x) = T\overline{F}(x) \qquad (35)$$

where α is the phase advance per unit cell which relates the fields on the two sides of a unit cell. T is the one dimensional transfer matrix of a NIM slab

$$T = \begin{pmatrix} T_{11} & T_{12} \\ T_{21} & T_{22} \end{pmatrix} = \begin{pmatrix} \cos(nk_0 d) & -\frac{z}{k_0}\sin(nk_0 d) \\ \frac{z}{k_0}\sin(nk_0 d) & \cos(nk_0 d) \end{pmatrix} (36)$$

with k_0 being the wave number of light in free space, *z* being the wave impedance of a slab and *n* being the refractive index. From (35) and (36), dispersion relation is given by solving

$$T_{11}T_{22} - e^{i\alpha d}(T_{11} + T_{22}) + e^{i2\alpha d} - T_{12}T_{21} = 0 \quad (37)$$

The elements of the transfer matrix can be expressed in terms of S parameters

$$T_{11} = \frac{(1+S_{11})(1-S_{22})+S_{21}S_{12}}{2S_{21}} \qquad (38)$$

$$T_{12} = \frac{(1+S_{11})(1+S_{22})-S_{21}S_{12}}{2S_{21}} \qquad (39)$$

$$T_{21} = \frac{(1-S_{11})(1-S_{22})-S_{21}S_{12}}{2S_{21}} \qquad (40)$$

$$T_{22} = \frac{(1-S_{11})(1+S_{22})+S_{21}S_{12}}{2S_{21}} \qquad (41)$$

Figure (9) shows the schematics of a homogeneous bianisotropic material slab that is placed in an open space. There are two different situations to be considered, i.e., wave incidence in the $+x$ and $-x$ directions. After applying the boundary continuous conditions, it is easy to obtain the expressions for the S parameters by using the transfer matrix method [20]. When the incidence is in the $+x$ direction as shown in Figures (7) and (9a), the corresponding reflection (S_{11}) and transmission (S_{21}) coefficients are as

$$S_{11} = \frac{2i\,sin(nk_0 l)[n^2+(\xi_0+i\mu_y)^2]}{\left[(\mu_y+n)^2+\xi_0^2\right]e^{-ink_0 l}-\left[(\mu_y-n)^2+\xi_0^2\right]e^{ink_0 l}} \qquad (42)$$

$$S_{21} = \frac{4\mu_y n}{\left[(\mu_y+n)^2+\xi_0^2\right]e^{-ink_0 l}-\left[(\mu_y-n)^2+\xi_0^2\right]e^{ink_0 l}} \qquad (43)$$

where l is the thickness of the homogeneous bianisotropic material slab and k_0 is the wave number of light in free space. For the case when the incidence is in the $-x$ direction, as shown in Figure (9b), we obtain the corresponding reflection ($S22$) and transmission ($S12$) coefficients as

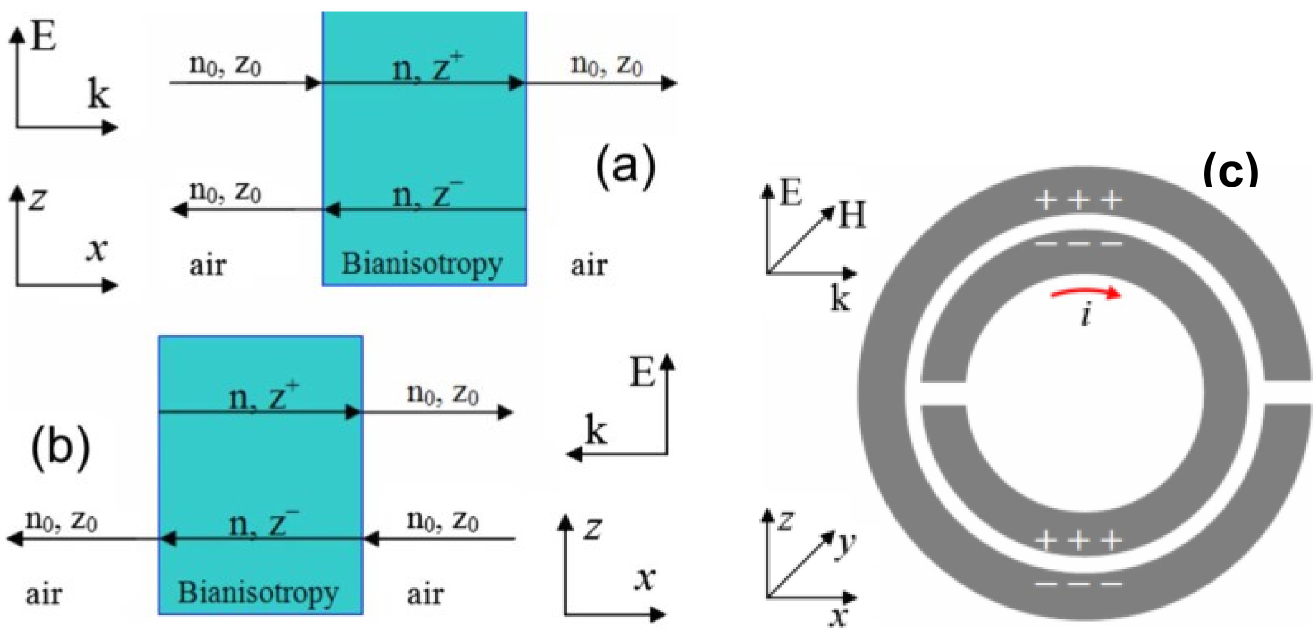

Fig.9. Schematics of a homogeneous bianisotropic slab placed in open space for the calculation of S parameters: (a) and (b) are for plane wave's incident in the $+x$ and $-x$ directions, respectively, (c) NMIS unit cell.

$$S_{12} = \frac{4\mu_y n}{\left[(\mu_y+n)^2+\xi_0^2\right]e^{-ink_0 l}-\left[(\mu_y-n)^2+\xi_0^2\right]e^{ink_0 l}} \qquad (44)$$

$$S_{22} = \frac{2i\, sin(nk_0 l)[n^2+(\xi_0-i\mu_y)^2]}{\left[(\mu_y+n)^2+\xi_0^2\right]e^{-ink_0 l}-\left[(\mu_y-n)^2+\xi_0^2\right]e^{ink_0 l}} \qquad (45)$$

From (43)-(45), S_{21} is equal to S_{12}, but S_{11} is not equal to S_{22}. There are 3-independent equations to for the 3-unknowns (n, μ_{yy} and ξ_0. By solving analytically (43)-(45), the expression for refractive index n is given by

$$\cos(nk_0 d) = \cos(\alpha d) = \frac{1-(S_{11}S_{22})+S_{21}^2}{2S_{21}} \qquad (46a)$$

From (36), using the condition of determinant (T) = 1, and substituting (38)-(41):

$$\cos(nk_0 d) = \cos(\alpha d) = \frac{1-(S_{11}S_{22})+S_{21}^2}{2S_{21}} \qquad (46b)$$

It is understood that when S_{11} is equal to S_{22}, (46) will degenerate into a standard retrieval form [2]. The refractive index n can be obtained from the implicit expression (46), which has many solutions for n to the different branches of the inverse cosine. When solving for n from (46), one must determine one branch from many branches of solutions. For a passive medium, the solved n must obey the condition$n'' = Im(n) \geq 0$, after computing n, other constitutive parameters is given as

$$\xi_0 = \left(\frac{n}{-2\, sin(nk_0 l)}\right)\left(\frac{S_{11}-S_{22}}{S_{21}}\right) \qquad (47)$$

$$\mu_y = \left(\frac{in}{sin(nk_0 l)}\right)\left(\frac{2+S_{11}+S_{22}}{2S_{21}} - cos(nk_0 l)\right) \qquad (48)$$

$$\mathcal{E}_z = \left(\frac{n^2+\xi_0^2}{\mu_y}\right) \qquad (49)$$

Consequently, impedances _z+ and z− can be obtained from (29)-(30). For a passive medium, following conditions should be satisfied $z^{+\prime} = Re(z^+) \geq 0$, $z^{-\prime} = Re(z^-) \geq 0$.

From (47)-(49), retrieved effective constitutive parameters can be assigned to NIM structure. However, variety of artifacts exists in the retrieved material parameters that are related to the inherent inhomogeneity of the NIM structure. The artifacts in the retrieved material parameters are particularly severe for NIM structure that make use of resonant elements, as large fluctuations in the index and impedance can occur, such that the wavelength within the material can be on the order of or smaller than the unit cell dimension. The retrieval technique based on analyzing the S-parameter of a finite slab can suffer from unphysical anti-resonances with a negative imaginary part for some of the parameters; these anomalies could be due to periodicity of the structure and spatial dispersion [11]-[12].

An example of this behavior can be seen in the retrieved imaginary parts of ε and μ, which typically differ in sign for a unit cell that has a magnetic or an electric resonance. In homogeneous passive media, the imaginary components of the material parameters are restricted to positive values. This anomalous behavior vanishes as the unit cell size approaches zero [2]. For a homogeneous or symmetric material, the value of z will be unique, while it will result in two different values for an inhomogeneous or asymmetric material. The impedance z is an intrinsic parameter which relates the electric field to the magnetic field as $= \frac{\bar{E}}{\bar{H}'}$.

From (35), two equivalent expressions for the impedance of a slab can be obtained by

$$z = \frac{T_{12}}{e^{i\alpha d} - T_{11}} = \frac{e^{i\alpha d} - T_{22}}{T_{21}} \qquad (50)$$

From (37) and (50)

$$Z^{\pm} = \pm \frac{(T_{11}-T_{22}) \pm \sqrt{(T_{22}-T_{11})^2 + 4T_{12}T_{21}}}{2T_{21}} \quad (51)$$

From two roots of (51) correspond to the two propagation directions of a plane wave. Substitution of (38)-(41) into (50) leads to

$$Z^{\pm} = \pm \frac{(S_{11}-S_{22}) \pm \sqrt{(1-S_{11}S_{22}+S_{12}S_{21})^2 - 4S_{12}S_{21}}}{(1-S_{11})(1-S_{22}) - S_{12}S_{21}} \qquad (52)$$

From (51) and (52), characteristic impedance which associates with a metamaterial with bianisotropic structures in terms of *S* parameters. For a passive medium the impedance needs to satisfy the conditions $(z^{+})' \geq 0$ and $(-z^{-})' \geq 0$, where $(\cdot)'$ denotes the real part operator.

For an example, a typical array of SRRs printed on substrate and unit cell is shown in Figure (10). As illustrated in Figure (10a), a plane wave is incident in the *x* direction and polarized in the *z* direction. For numerical example, the dimensions as *a* = 3 mm, *r* = 0:74 mm, *c* = 0:2 mm, *s* = 0:1 mm, *g* = 0:2 mm, *t* = 0:3 mm, *h* = 35 mm; and permittivity of the substrate is ε_0 for simplification [13].

It can be seen from Figures (10b) and (10c) that S_{12} is equal to S_{21} and the magnitudes of S_{11} and S_{22} are almost the same, while the phase of S_{11} is different with that of S_{22}. In this case, the application of the standard retrieval method [1] will lead to an inaccurate result.

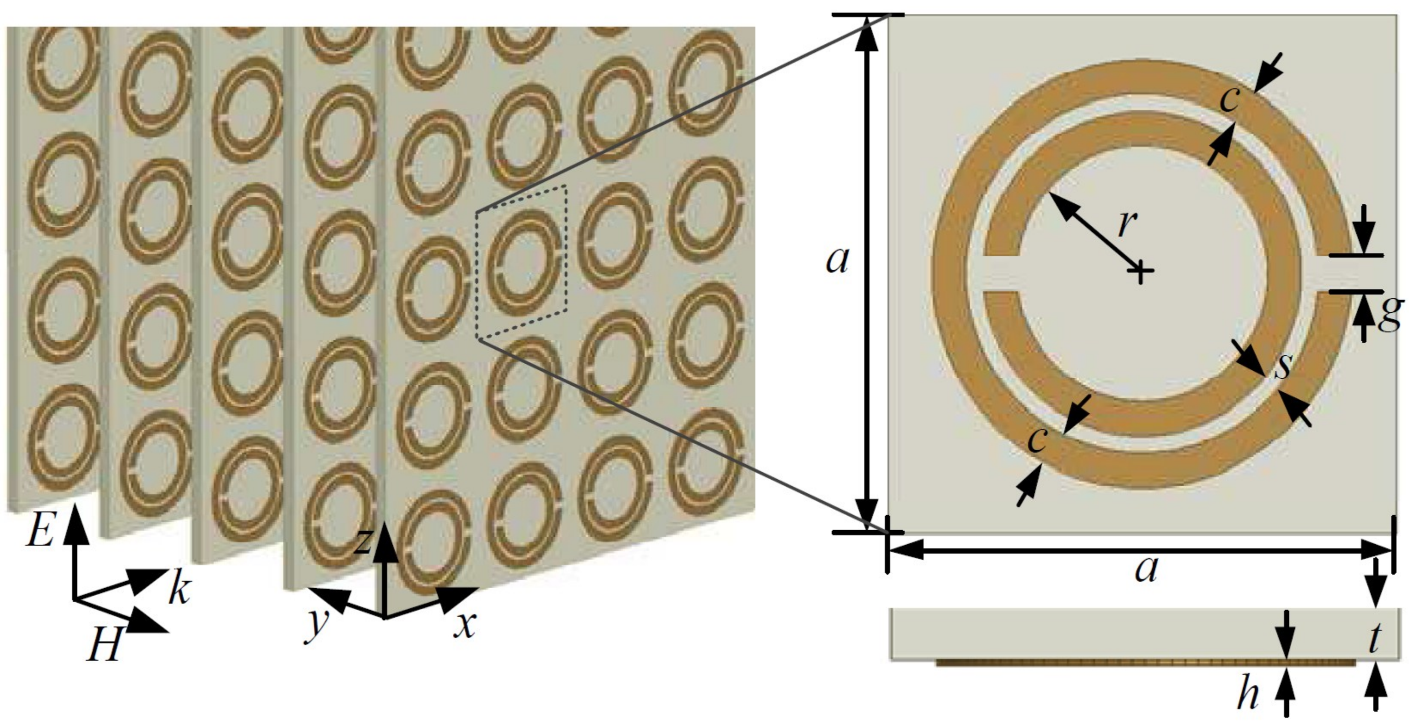

(a) Array of SRRs printed on substrate (b) SRR unit cell

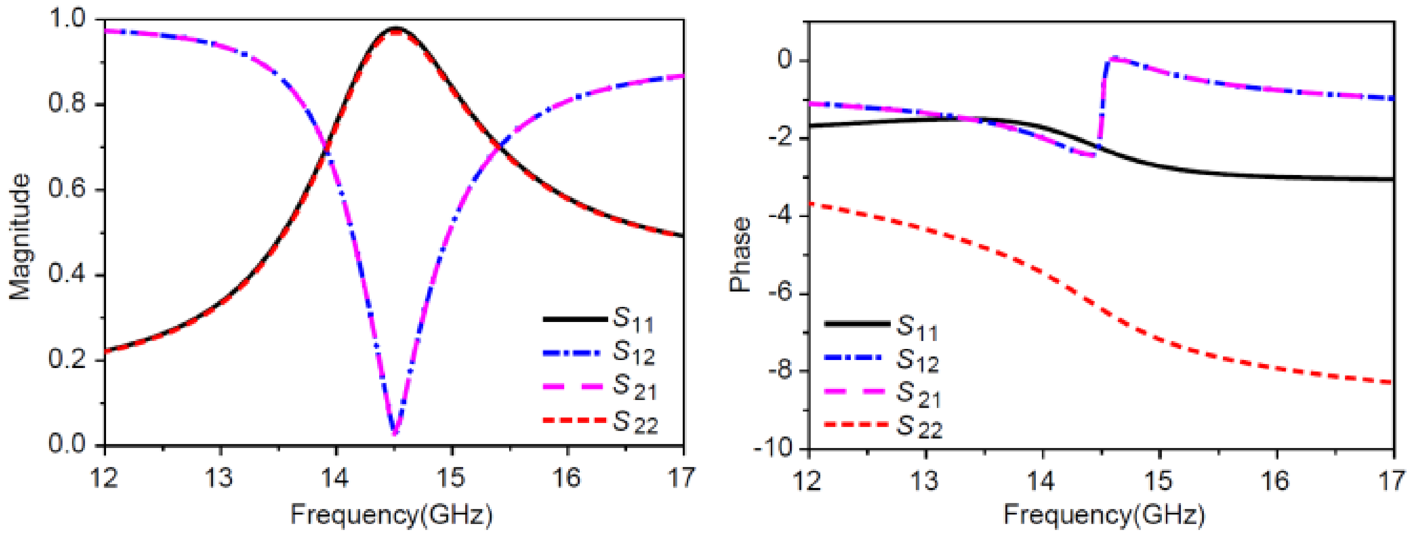

(c) Magnitude: S-parameters (d) Phase: S-parameters

Fig.10: A typical bianisotropic structure: (a) array of SRRs printed on substrate with the metallization in yellow, (b) SRR unit cell, (c) magnitude of S-parameters, and (d) phase of S-parameters [13]

The discrepancy in phase of S parameter measurement is because of the fact that the NIM's cells are not infinitely small compared to the incoming wavelength, causing space dispersion.

Assuming that there is a plane wave propagating in the direction of +*x,* polarized in the +*z* direction. The constitutive relationship between electric field and magnetic field can be described as

$$\overline{\mathrm{D_z}} = \varepsilon_0 \varepsilon_z \overline{E_z} - ic^{-1}\xi_0 \overline{H_y} \quad (53)$$

$$\overline{\mathrm{B_y}} = \mu_0 \mu_y \overline{H_y} + ic^{-1}\xi_0 \overline{E_z} \quad (54)$$

With the substitution of (53)-(54) into Maxwell's equations (18)-(19):

$$\nabla^2 \overline{E_z} + \omega^2 \varepsilon_0 \mu_0 \left(\varepsilon_z \mu_y - \xi_0^2\right) \overline{E_z} = 0 \quad (55)$$

From (13), the index (n) can be given by

$$n^2 = \varepsilon_z \mu_y - \xi_0^2 \quad (56)$$

For a passive material, the roots have to be chosen properly to guarantee the condition $Im(n) \geq 0$ Otherwise, the exponentially growing solutions will occur, which violates the energy conservation. The impedances of a bianisotropic material for the wave propagation in the right-hand or left-hand directions are $Z^{\pm}$, the values of which are given by the equations $Z^{+} = \frac{E^{+}}{H^{+}}$ and $Z^{-} = \frac{E^{-}}{H^{-}}$.

From Maxwell's equations (18)-(21), the formulas of the impedance and effective parameters s can be obtained,

$$Z^{\pm} = \frac{Z^{\pm}}{Z_0} = \frac{\mu_y}{\pm n - i\xi_0} \;, Z_0 = \sqrt{\frac{\mu_0}{\varepsilon_0}} \qquad (57)$$

$$\varepsilon_z = \frac{n + i\xi_0}{Z^+} \qquad (58)$$

$$\mu_y = (n - i\xi_0)Z^+ \qquad (59)$$

$$\xi_0 = in\frac{Z^- + Z^+}{Z^- - Z^+} \qquad (60)$$

The refractive index of and impedances for a bianisotropic medium can be obtained from (46) and (52). The expressions for the effective electromagnetic parameters (ε_z, μ_y and ξ_0) and impedance associate with the bianisotropic structure such are given from (58)-(60), can be used for designing NIMS resonator for next generation energy efficient signal sources.

III. NIMs Inspired Resonator For Oscillator Circuit

NIMs resonator can be classified into two types: resonant type and non-resonant type: examples are Split Ring Resonator (SRR), and Left Handed (LH) Transmission Line (T-line). Resonant type metamaterial exhibit larger dynamic range for material parameter ($\varepsilon_r < 0$, $\mu_r < 0$), while non-resonant type offers wide bandwidth and lower loss. Traditional metamaterial transmission lines (T-lines) can also be categorized into resonant type and non-resonant type, represented by (split-ring-resonator) SRR/(complementary split-ring-resonator) CSRR loaded T-line, and Composite Right/Left Handed (CRLH) T-line, with the corresponding layout shown in Figures (11) and (12), where *C* and *L* are per-unit length capacitance and inductance that determine the metamaterial properties of T-lines. For T-line loaded with SRR (Fig. 1), L_1 and C_2 linked with T-line, whereas C_1 and L_2 are linked to magnetic coupling. Figure (11) shows the typical split ring resonator and the construction of NIM.

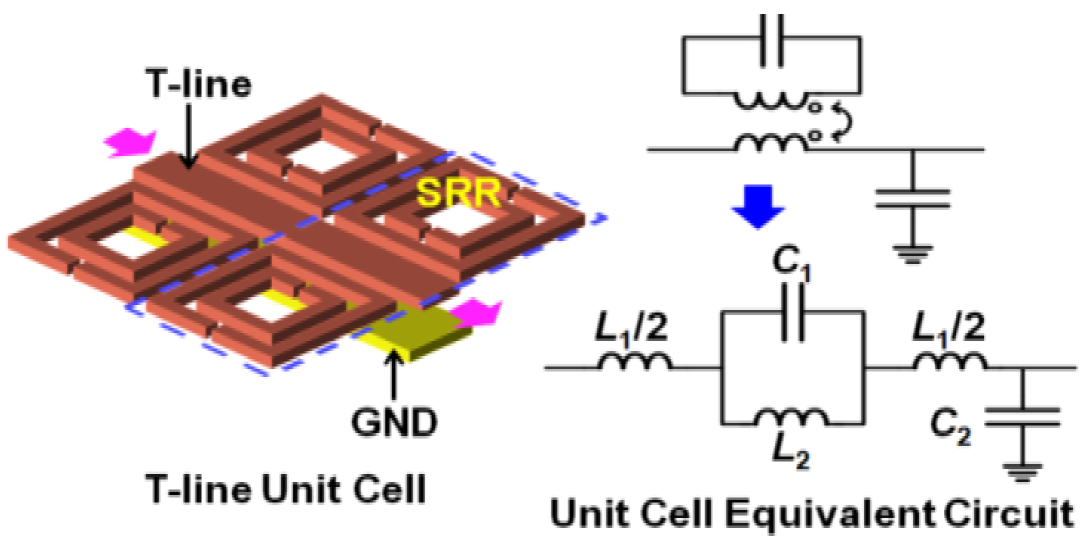

Fig.11: SRR loaded T-line unit cell and equivalent lumped LC model

The physical properties of Figure (11) are given by:

$$\varepsilon = \frac{Y}{j\omega} = C_2 \text{ is} + \text{ve} \rightarrow \varepsilon > 0\ (+ve) \qquad (61)$$

$$\mu = \frac{Z}{j\omega} = \frac{L_1+L_2-\omega^2 L_1 L_2 C_1}{1-\omega^2 L_2 C_1} \qquad (62)$$

$$\mu < 0\ (-ve)\ \text{for}\ \left(\frac{1}{L_2 C_1}\right)^{1/2} < \omega < \left(\frac{L_1+L_2}{L_1 L_2 C_1}\right)^{1/2} \qquad (63)$$

From (61) and (63), Re (μ) is negative and Re (ε) is positive. For (ε>0, μ<0), propagating waves become evanescent waves, therefore energy cannot propagate through the resonator, reflected back to establish a standing-wave.

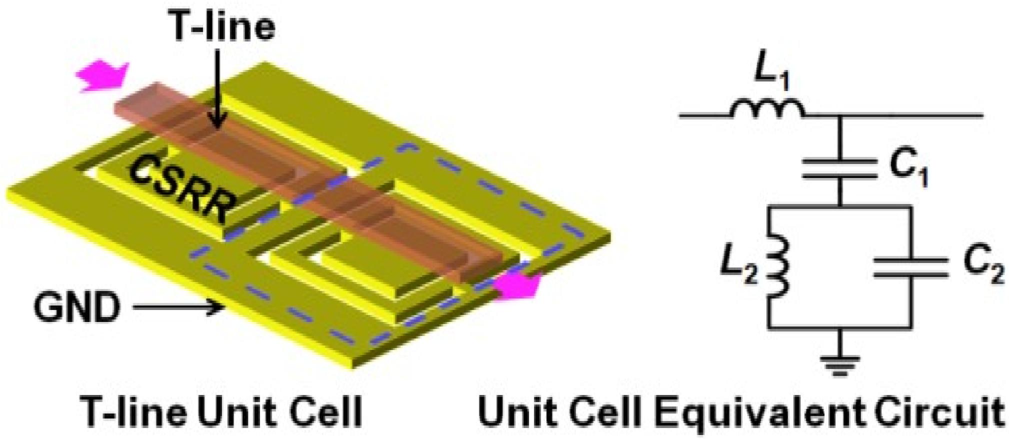

Fig.12: CSRR loaded T-line unit cell and equivalent lumped LC model

As a result, SRR loaded T-line structure stores the energy and forms a high-Q resonator tank circuit for low phase noise oscillator application. Similarly, for T-line loaded with CSRR (Fig. 12), L_1 associated with T-line, C_1, C_2, and L_2 account from electric coupling of CSRR on the ground.

The physical properties of Figure (12) are given by

$$\mu = \frac{Y}{j\omega} = L_1 \text{is} + \text{ve} \rightarrow \mu > 0\ (+ve) \qquad (64)$$

$$\varepsilon = \frac{Y}{j\omega} = \frac{C_1(1-\omega^2 L_2 C_2)}{1-\omega^2 (C_1+C_2) L_2} \qquad (65)$$

$$\varepsilon < 0\ (-ve)\ \text{for}\ \left(\frac{1}{(C_1+C_2)L_2}\right)^{1/2} < \omega < \left(\frac{1}{L_2 C_2}\right)^{1/2} \qquad (66)$$

From (64) and (66), Re (μ) is positive and Re (ε) is negative, In this case (ε < 0, μ > 0), electric plasma is formed, where propagating waves become evanescent waves, hence, energy cannot propagate through the resonator either and is reflected back to establish a standing-wave. As a result, CSRR loaded T-line can also be used to form a high-Q resonator.

Figure 13(a) shows the structure of the broadside-coupled split-ring resonator, there are two relative slips S_x and S_y between the two broadsides coupled rings. Figure 13(b) shows the corresponding equivalent circuit, where *L,R* are the equivalent inductance and resistance, respectively; C_0 is mutual capacitances between the two rings; C_s is the capacitance of the split. As shown in Figure (13a), the tuning can realize by minor slips along and perpendicular to the gap direction of two broadsides coupled rings [22]. Figure (14) shows the (a) layout of the broad coupled split ring (dark region denotes etched on signal plane, and light region denotes broadsides coupled triangular SR etched on ground plane), and (b) equivalent lumped circuit.

For the validation of reported research work, resonators were fabricated on low loss Quartz and Borosilicate material. As shown in Fig. (3), the metal structures are processed on top of quartz wafers (diameter D=150 mm). The fabrication process uses a double-side coating of the substrates using a metallization, sputtered metal gold (Au) is used.

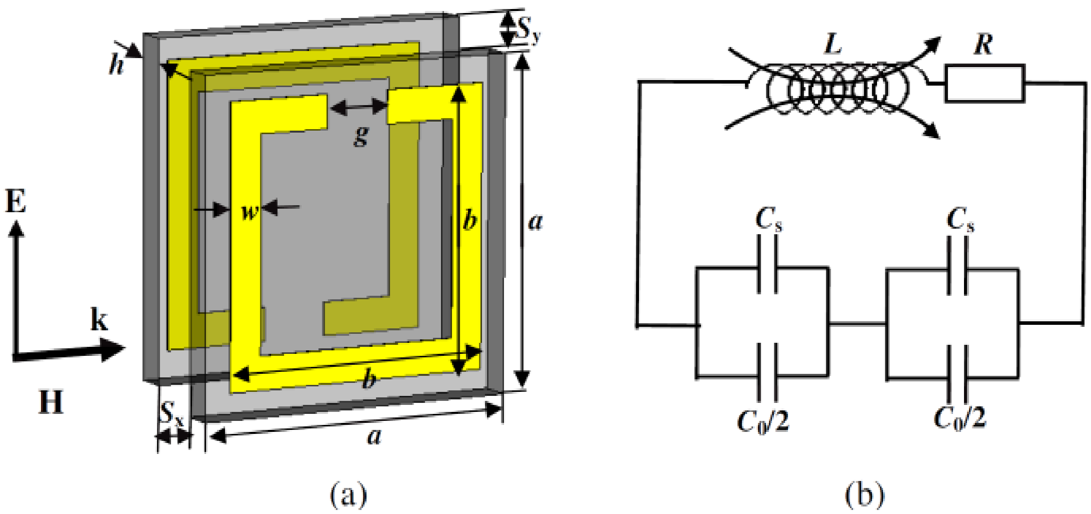

Fig.13: (a) A typical broadside-coupled split-ring resonator (b) equivalent lumped circuit representation [22]

Fig.14: (a) Layout of the BCTSR (dark region denotes BCTSR etched on signal plane, and light region denotes broadsides coupled triangular SR etched on ground plane) (b) equivalent lumped circuit

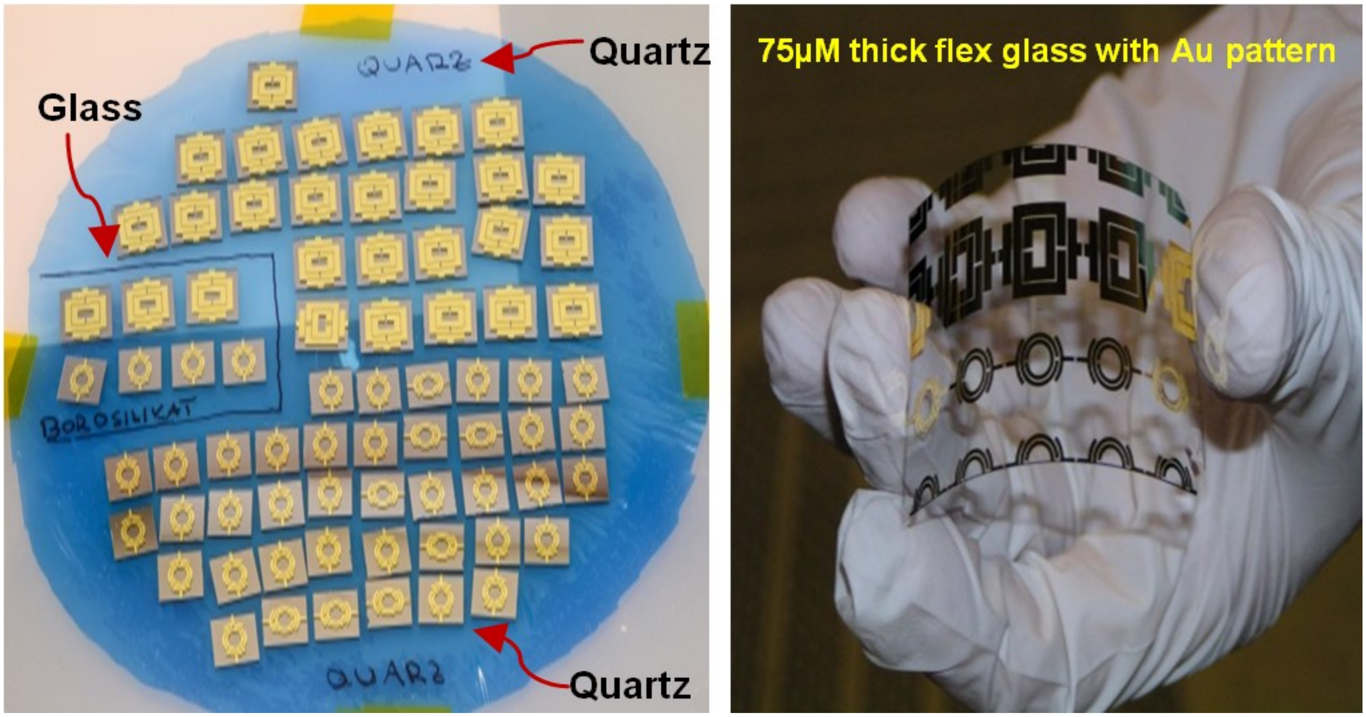

Fig.15: Photos of Metamaterial resonator fabricated on glass/quartz

Unlike SRR/CSRR as depicted in Figure (15), the geometry of Negative Index Möbius-Strips (NIMS) is conformal, continuous, and maps one-to-one onto it-self. These unique properties of NIMS permit EM coupling in such a way that signal coupled to loop does not encounter any obstructions when travelling around the loop, emulate like an infinite transmission line, hence large group delay and high Q-factor. In this paper, oscillator circuit uses negative index (ε_r <0, μ_r <0) NIMO (Negative Index Möbius Oscillator) circuit for low cost high performance solution.

IV. *Examples*

(a) Signal Source

MMI (Möbius Metamaterial Inspired) structures are artificially constructed media on a size scale smaller than wavelength of external stimuli, they can exhibit a strong localization and enhancement of fields, which may provide novel tools to significantly enhance the sensitivity and resolution of sensors, and open new degrees of freedom in sensing design aspect [1]-[10]. The detailed discussion about characteristics of MMI structure is given in Part-I (MWJ May Issue), this issue (Part-II) mainly presents the applications of MMI structure in high frequency signal sources and sensors, as well as their challenges and prospects [28].

From Part-I (MWJ May Issue, Equation 2 to 6, ref 28), Möbius transformation can be used for reducing the complexity of system of N-coupled oscillators [29].

Figure (16) shoes the typical N-coupled N-Push oscillator topology for the purpose of analysis [29].

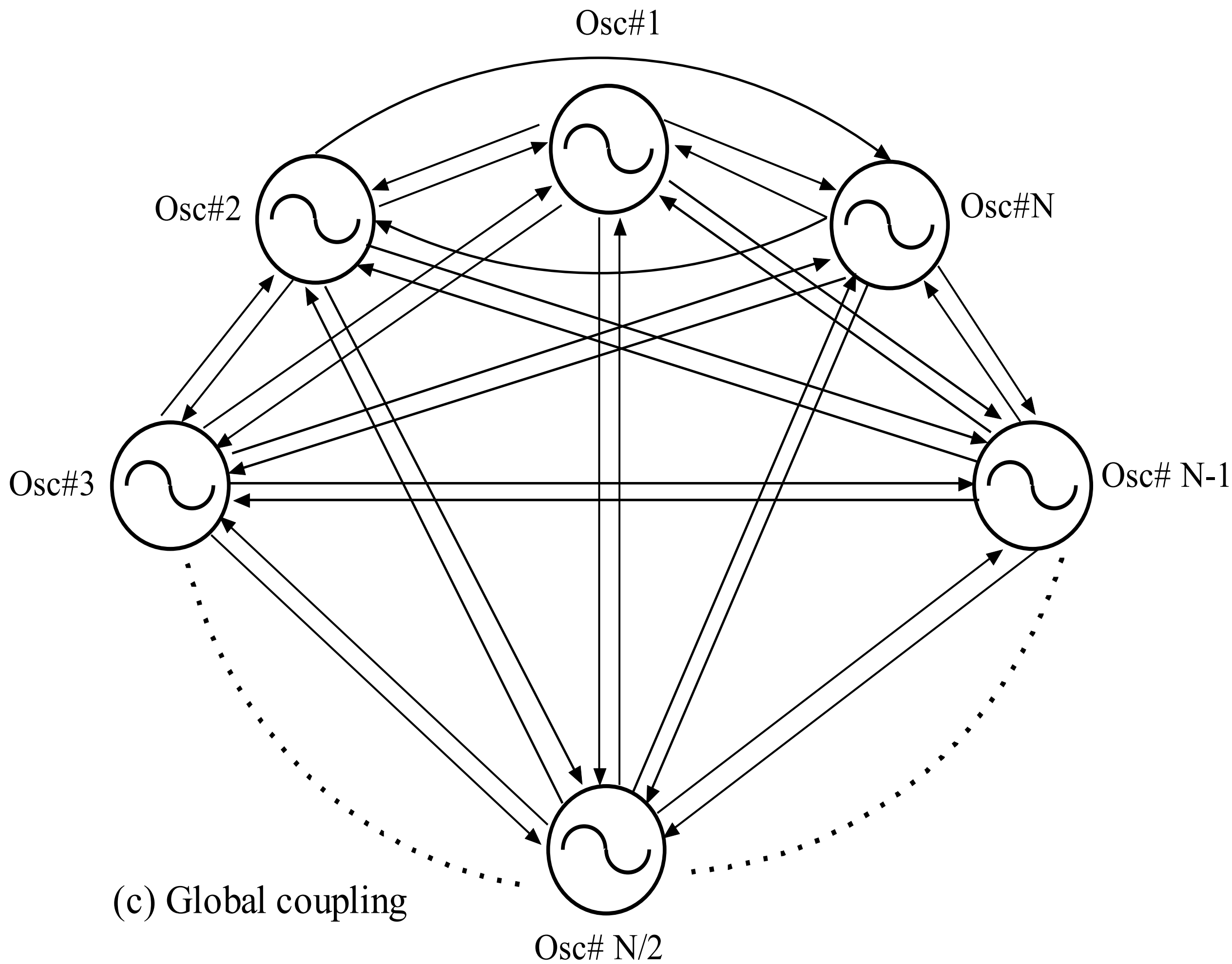

Fig.16: A typical N-coupled N-Pus oscillator topology [29]

Globally, coupled oscillators have been used to model many diverse systems in physics, biology, chemistry, engineering, and space science. The system of Coupled-oscillators exhibit complex behavior because of each individual unit influences the characteristics of other units. The phase dynamics of N-coupled oscillator shown in Figure (16) is described by [29]

$$\frac{\partial \theta_i(t)}{\partial t} = \omega_i - \left[\frac{\omega_i}{2Q_i}\right]\left[\sum_{\substack{j=1 \\ j\neq i}}^{N} \beta_{ij}\left(\frac{A_j(t)}{A_i(t)}\right)\sin[\theta_i(t) - \theta_j(t) + \varphi_{ij}]\right] - \left[\frac{\omega_i}{2Q_i} B_{ni}(t)\right] \; i = 1, 2, 3 \ldots N \tag{67}$$

where $A_i(t)$, $\theta_i(t)$, ω_i, and Q_i are the amplitude, phase, free-running frequency, and Q factor of the i^{th} oscillator, B_{ni} corresponds to the phase fluctuations, and β_{ij} and φ_{ij} are the coupling parameters between i^{th} and j^{th} oscillators.

From (67),

$$\frac{\partial \theta_i}{\partial t} = \dot{\theta}_i = f e^{j\theta_i} + l + \bar{f} e^{-j\theta_i} \quad \text{(for } i = 1, 2, 3 \ldots N\text{)} \tag{68}$$

where f is any smooth complex-valued 2π-periodic function of the phases $\theta_1,\ldots\ \theta_N$ and over bar ($\bar{f}$) is complex conjugate.

The coupled-oscillators system shown in Figure (16) tends to collective synchronization and lock to a common frequency, despite oscillators' difference in their natural frequencies. However, accurate solution of (67) and (68) become difficult due to nonlinearity and large number of variables associated with coupled-oscillator systems.

An alternative means to solve this by reducing the complex dynamics to phase models assuming the couplings among oscillators are sufficiently weak such that when oscillators are uncoupled, their phases advance at constant 'velocities' (natural frequency). The functions *f* and *l* given in (68) may depend on time and on any auxiliary state variables in the system, assuming such system sinusoidally coupled because the dependence on *i* occurs solely through the first harmonics $e^{j\theta_i}$ and $e^{-j\theta_i}$ [30]. This particular class of dynamical systems (68) can be reducible by a Möbius transformation to form [31]

$$e^{j\theta_i(t)} = M_t[e^{j\phi_i(t)}] \tag{69}$$

for i=1, 2, 3…N, where M_t is a one-parameter family of Möbius transformation and ϕ_j is a constant (time-independent) angle. The time-t flow map is an orientation-preserving homeomorphism, exhibits a Möbius map.

From (67) and (68), the distribution of natural frequencies for $N\rightarrow\infty$ given by the sum of two Lorentzian distributions $l\ (\omega)$ [31]:

$$l\ (\omega) = \frac{\Delta}{2\pi}\left(\frac{1}{(\omega-\omega_0)^2+\Delta^2} + \frac{1}{(\omega+\omega_0)^2+\Delta^2}\right) \tag{70}$$

where Δ is the width parameter (half-width at half-maximum) of each Lorentzian and $\pm\omega_0$ are their center frequencies, as depicted in Figure (17).

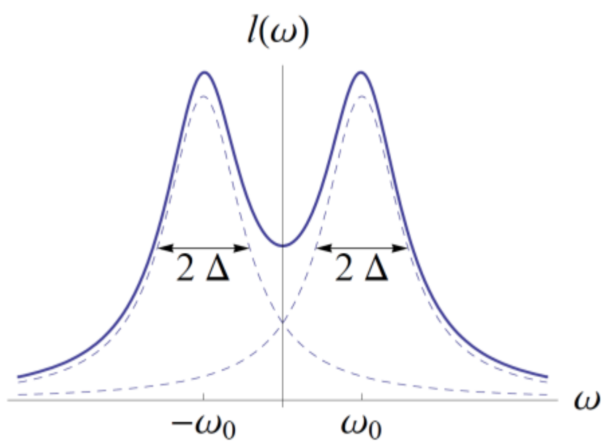

Fig.17. Bimodal distribution: consisting of sum of 2-Lorentzians [17]

From (70), the challenges are minimization of frequency detuning (proportional to separation between the two center frequencies) and AM-PM conversion noise. For low noise oscillator applications, resonator Q-factor is important parameter. Resonator network formed with Möbius-Strips are conformal, continuous, and maps one-to-one onto itself; therefore signal coupled to strips do not encounter any obstructions while travelling around the strip in such a way that the loop made of strips would act like an infinite transmission line. This arrangement enables large group delay and improved Q-factor, therefore promising for filter and oscillator applications. Möbius-Strips can have more than 1-twist (Fig. 13, May Issue Part-I, ref 28). The 3-twisted Möbius-Strip will have the trefoil knot as the boundary curve and so on. It is interesting to analyze the geometric phase of multi-knots non-orientable surfaces (Möbius) and their connection with nonlinear dynamical systems. This may provide a diagnostic analysis in abnormal neural oscillations and synchrony in schizophrenia.

Figure (18) illustrates the typical phase-injection mechanism using phase-perturbation at i^{th} node on Möbius-Strips resonator based frequency generating electronic circuits.

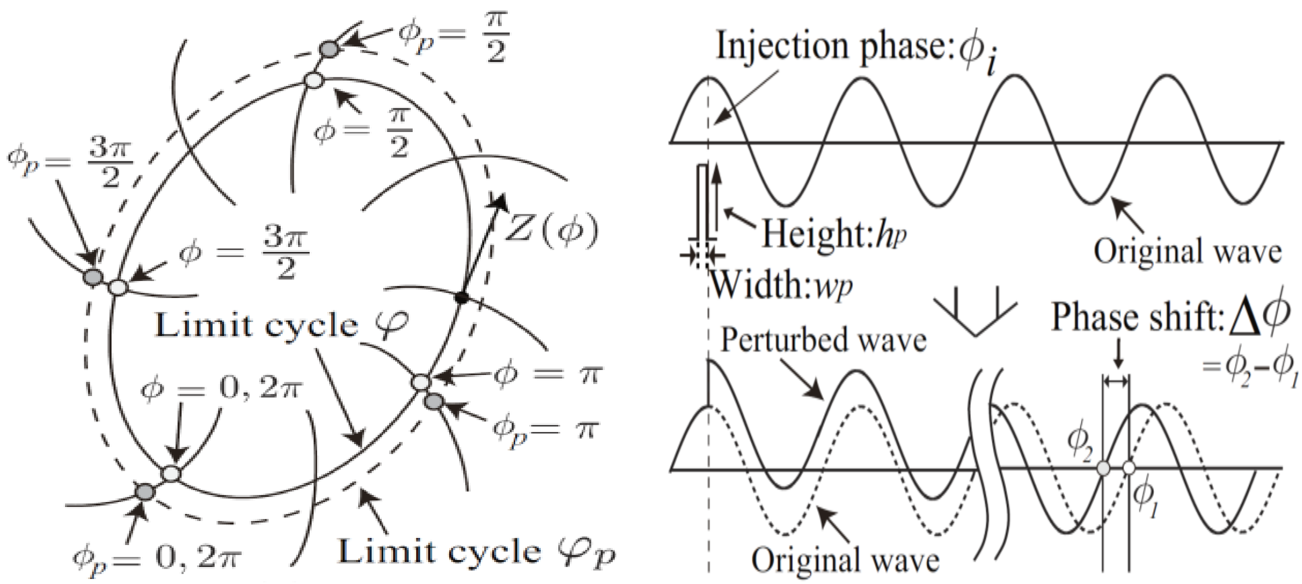

Fig. 18: Shows the typical phase-injection mechanism in Möbius strips resonator due to perturbation at i^{th} node

The Q-factor (Q_L) of resonator is [29]:

$$Q_L = \frac{\omega_0}{2}\left|\frac{d\varphi(\omega)}{d\omega}\right|_{\omega=\omega_0} = \frac{\omega_0}{2}\tau_d; \quad \tau_d = \left|\frac{d\varphi(\omega)}{d\omega}\right|_{\omega=\omega_0} \tag{71}$$

$$\tau_d = \left.\frac{d\varphi(\omega)}{d\omega}\right|_{\omega=\omega_0} = \frac{\varphi(\omega_0+\Delta\omega)-\varphi(\omega_0-\Delta\omega)}{2\Delta\omega} \tag{72}$$

where $\varphi(\omega)$ is the phase of the resonator impedance and τ_d is the group delay. The effective inductance of the Möbius strips varies with the current/voltage passes through strips, building evanescent field, therefore higher quality factor:

$$\overline{Q_m(\omega)}_{\omega\to\omega_0} = \left[\frac{\omega}{2(I_{max}-I_{min})}\int_{I_{min}}^{I_{max}} Q_m(\omega.i)\,di\,\right]_{\omega\to\omega_0} \tag{73}$$

where I_{min} and I_{max} are the minimum and maximum currents, and $Q_m(\omega,i)$ is the instantaneous quality factor at frequency ω and current i flow through Möbius strips resonator.

From Figure (18), the locking condition given by

$$\frac{2(f-f_0)}{f} = \frac{\eta\sin(\phi)}{2+\cos(\phi)} \tag{74}$$

From (74), locking range restricted by the phase shift [30]:

$$\Delta f = \frac{f_0}{2Q}\tan\left(\sin^{-1}\left(\frac{\eta}{2}\right)\right) \tag{75}$$

where f_0, Q, and η are the resonant frequency, quality factor of the LC tank, and the injection ratio (i_{inj}/I_{DC}) respectively.

Using Equations (71)-(75), 25 GHz multi-knots Möbius-Strips resonator based oscillator designed and validated. Figure (19) shows the PCB layout of 25 GHz Möbius-Strips resonator oscillator, fabricated on 8-mil thick Roger substrate, with dielectric constant value of 2.2.

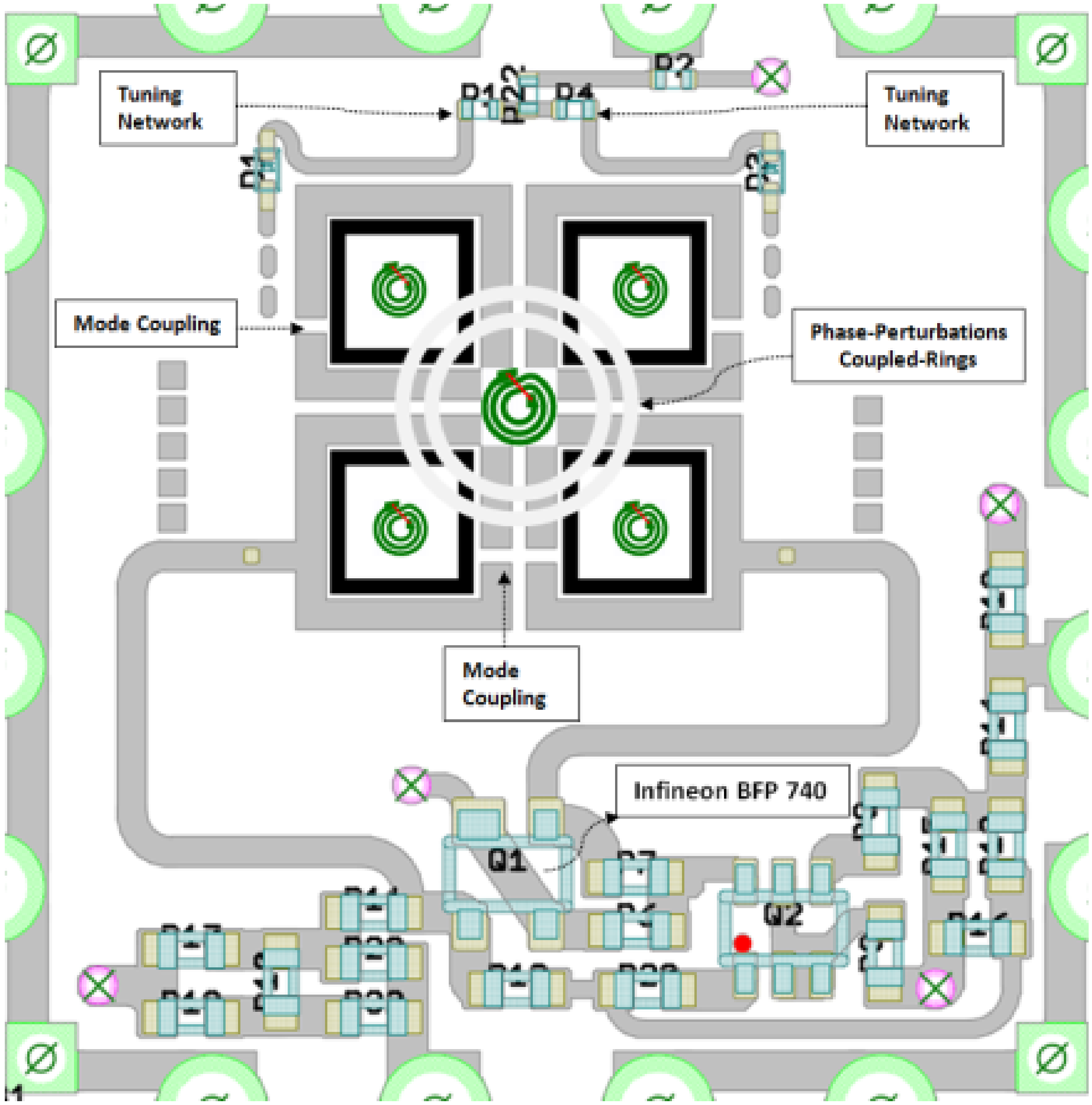

Fig. 19: A typical layout of 25 GHz oscillator using Möbius coupled resonator

As shown in Figure (19), the Möbius-Strips resonator causing increase in evanescent mode field energy conservation due to invariance of solutions for strips under a 2π rotation with a definite handedness. The resonator coupling coefficient 'β_j' depends upon the geometry of the perturbation:

$$\beta_j = \left[\left(\frac{\int \varepsilon E_a.E_b dv}{\sqrt{\int \varepsilon E_a^2 dv \int \varepsilon E_{bd}^2 dv}}\right)_e + \left(\frac{\int \mu H_a.H_b dv}{\sqrt{\int \mu H_a^2 dv \int \mu H_b^2 dv}}\right)_m\right] \tag{76}$$

where E_a and H_a are the electric and magnetic field produced by the Möbius strip, and E_b, H_b are the corresponding fields due to perturbation or nearby adjacent resonator, subscript 'e' and 'm' are the electrical and magnetic coupling.

Figure (19) shows the circuit layout of tunable oscillator using Multi-knots Möbius-Strips resonator, which support multi-injection nodes, thereby minimize the detuning and provides mechanism to suppress the noise of oscillator circuits. The influence of phase-injections (perturbations) at different nodal points on Möbius-Strips resonator are discussed for improving the tuning-range and phase noise performance of frequency generating circuits. The oscillator circuit shown in Figure (19) works at DC bias of 5 Volt and 68 mA, measured output power is typically -6 dBm.

Figure (20) shows the measured phase noise plot of -109dBc/Hz @ 10 kHz offset with o/p power -6.73dBm and 500 kHz tuning. The major drawback of this topology is limited tuning and mode-jumping.

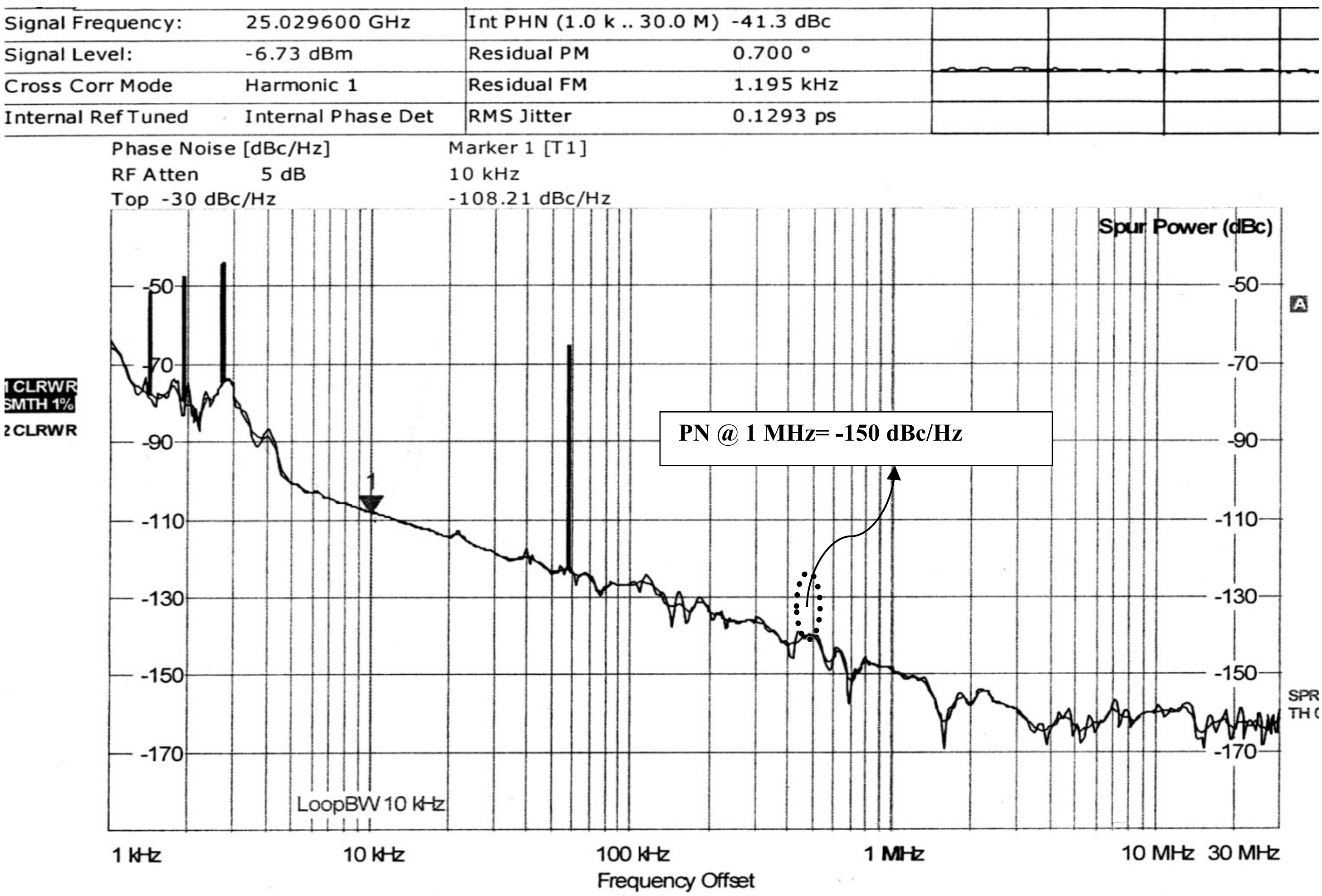

Fig.20 Measured Phase Noise Plot of 25 GHz oscillator prototype (Fig.19)

For practical applications, o/p power, frequency stability, and tuning range need to be improved. These problems can be partially or fully fixed by understanding the phasor relationship between ring and Möbius strip resonator. Figure (21) shows the typical representation of ring and Möbius strips resonator, and equivalent LC representation consisting of *L* and *C* along the transmission line. By virtue of Möbius transformation, strips exhibit large group-delay, well suited for microwave resonator applications.

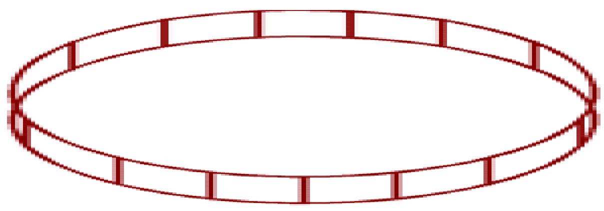

(a) Ring Resonator

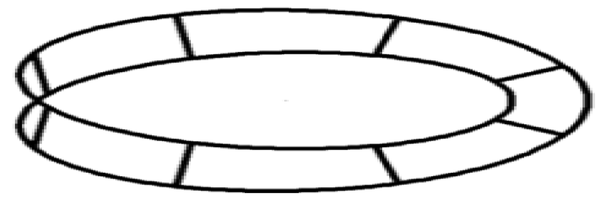

(b) Mobious Strip

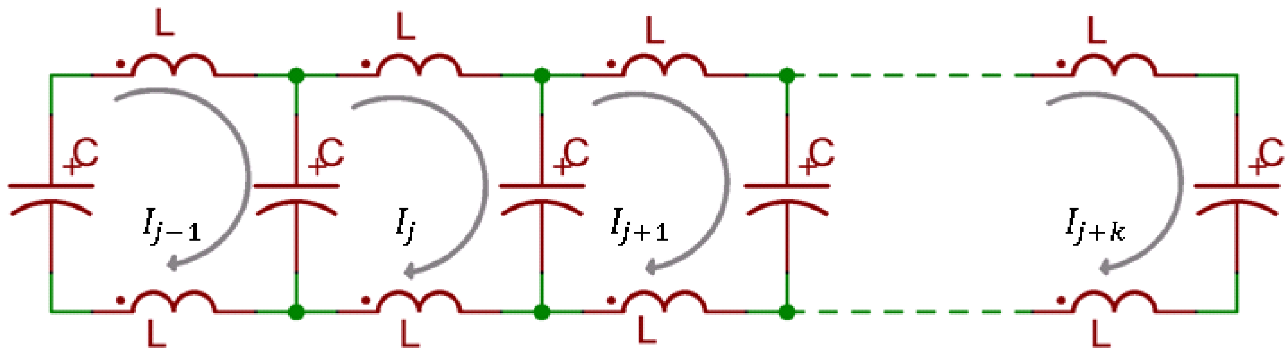

(c) Equivalent LC representation consisting of *L* and *C* along the transmission line

Fig.21: (a) the ring resonator (b), the Möbius strip, and (c) equivalent LC representation consisting of *L* and *C* along the transmission line

The electric currents on the ring resonator as shown in Figure 21(c) can be formulated by a periodic boundary condition of the form described by

$$I_{j+k} = I_j \tag{77}$$

where I_k represents the electric current around the n^{th} closed loop on the periodic ladder structure of *k*-elements.

The boundary condition of the general form shown in (77) governs that I_k are a conserved quantity that gives invariance of solutions under a 2π rotation with a definite handedness. The non-dissipative wave equation of LC network shown in Figure (21c) for the k^{th} element:

$$I_k = A_1 e^{\left(\frac{p2\pi k\mathrm{M}}{k}\right)} + A_2 e^{-\left(\frac{p2\pi k\mathrm{M}}{k}\right)} \tag{78}$$

$$\left(\omega^2 - \frac{1}{LC}\right) I_k - \left(\gamma\omega^2 - \frac{1}{2LC}\right)(I_{k+1} + I_{k-1}) = 0 \tag{79}$$

$$\omega^2 = \left\{\frac{2sin^2\left(\frac{p\pi}{k}\right)}{LC\left(1-2\gamma cos\frac{2p\pi}{k}\right)}\right\} \tag{80}$$

where *p* is an integer specifying the normal mode, γ is mutual coupling coefficient (mutual inductance 'M'=2γL), *k* is number of element structure. From (77)-(80), for even value of *k*, there are *k*-1 eigenvalues, including (*k*-2)/2 degenerate doublet and one singlet.

A typical ring resonator, whose Eigen functions satisfy (17), defines a distinct inner and outer surface of the ring, shown in Fig.(21a).

Figure (21c) shows a topological transformation resulting in a Möbius strip resonator, whose current dynamics formulated by applying twisted boundary condition as

$$I_{j+k} = -I_j \tag{81}$$

From (81), a simple topological transformation on the resonator ring (Fig. 21b) results in a sign reversal of current (I_j) upon a 2π rotation of the solutions, and a 4π rotation is now required for invariance of the Eigen functions.

Note that the eigenfunctions satisfying the condition for twisted boundary are of the same form as (77) provided that the mode indices are given half-integral values (p = 1/2, 3/2, 5/2,…(k-1)/2) relative to a ring consisting of identical components. The dispersion relation for Möbius ring is same as (80), however, the wave-vectors are shifted by

$$\Delta\lambda = -\left(\frac{\pi}{k}\right) \tag{81}$$

From (80)-(81), two distinct topologies shown in Figures 21(a) and 21(b) can be considered as a complementary pair related by a single transformation. The eigenfunctions of the Möbius resonator form an orthogonal basis set; presents an interesting possibility for the design of Metamaterial for the application in multi-phase oscillator circuits. The inherent multi-phase, multi-mode nature of the Möbius strip provides additional degrees of freedom relative to traditional designs for generating multi-phase and quadrature oscillators, which are essential modules of many electronic systems, such as image rejection demodulator in wireless transreceivers, half-rate clock-data-recovery (CDR) circuitry in high-speed optical receivers, phased-arrays, direct-conversion transmitter, and fractional-N frequency synthesizers. Figure (22) shows the typical ring oscillator, exhibits multi-phase but it suffers from high phase noise [31].

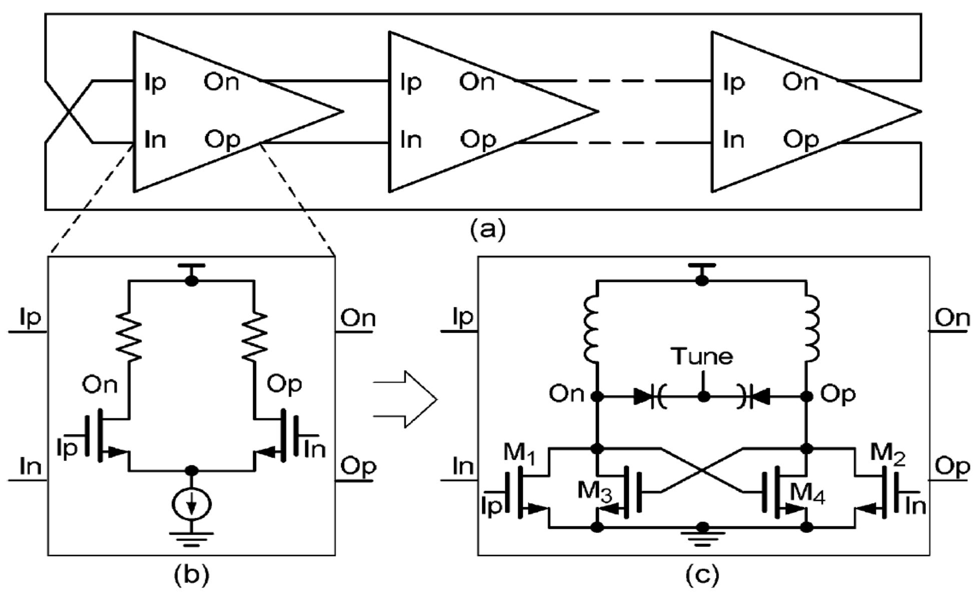

Fig. 22: Ring oscillator: (a) general structure, (b) purely active gain stage, and (c) LC-boosted gain stages [32]

LC-boosted ring oscillator as shown in Fig. 22(c) minimizes the noise but still inferior to single-stage *LC* oscillator, largely due to the trade-off between phase noise and phase error. Strong coupling between the gain stages (implies large-coupling MOSFETs) can minimize the phase errors; on the other hand, large coupling MOSFETs will increase noise and power consumption [31]. In all possible multi-phase *LC* oscillator configurations, MOSFETs play a dual role: compensate the energy loss in *LC* tanks, and couple *LC* tanks together and maintain a desired phase relation [32]. However, the second goal deteriorates phase noise, especially 1/f (flicker) noise up-conversion [33]. These problems can be partially of fully overcome by replacing MOSFETs with Metamaterial Möbius connected high order LC ring resonator in distributed topology, shown in Figure (23). The resonant frequency of Metamaterial (-ve index material) LC-ring resonator increases with the number of stages *N* as compared to right-handed (+ve index material) LC-ring resonator. Therefore, Metamaterial LC-ring resonator is well suited for high frequency generation.

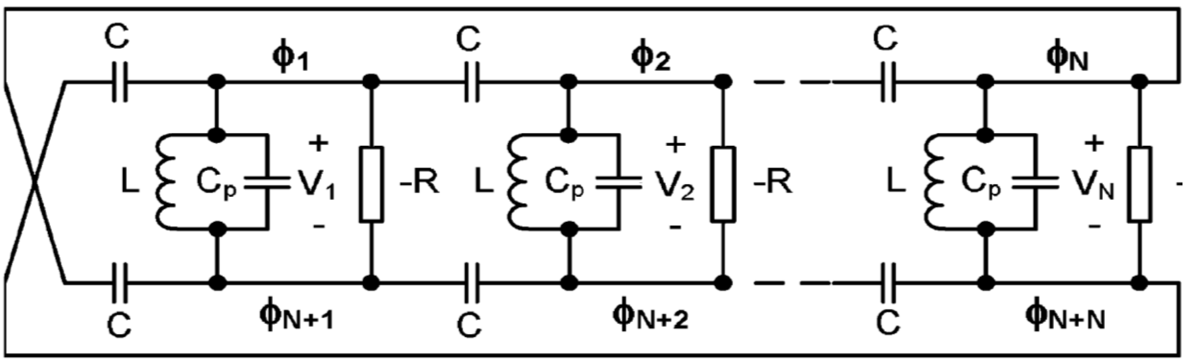

Fig. 23: A typical negative index Möbius-connected LC-ring oscillator [33]

As shown in Figure (23), MOSFETs acts as negative resistance generating devices, needed only for compensating the loss of the LC-ring resonator, implies that current from MOSFETs are always injected into the resonator in phase with voltage and do not resonate with LC resonator components. For N-stage distributed LC-ring oscillator, the phase noise scales down as 1/N, while the power consumption increases linearly with N. This allows synthesizing multi-phases, while maintaining the identical figure of merit (FoM) as a 1-stage *LC* oscillator [34]. The main challenges of these topologies are mode selections and desired phase relations. In addition to this, assumption for number of noise sources increases linearly with *N*, the total phase noise should be proportional to 1/N no longer hold good under large signal drive level condition. The alternative approach is wave-based Möbius oscillator. The energy recycling nature of Möbius strips allows very high frequencies oscillations with minimum power consumption for a given class of frequency generating circuits.

Figures 24(a) and 24(b) show the differential open ring and closed cross-connected ring. When the voltage source connected in Figure 24(a) replaced by a cross-connection of the inner and outer conductors, leads to a signal inversion. If there were no losses, a wave could travel on this differential ring indefinitely, providing a full clock cycle every other rotation of ring, defined as Möbius effect [35]. However, in real applications, multiple anti-parallel inverter pairs added to the line shown in Figure 24(c) to overcome losses and provide rotation lock of Möbius connected differential ring.

Figure (25) shows the lumped equivalent of coupled stripline used for Möbius ring described in Figure (24) [36].

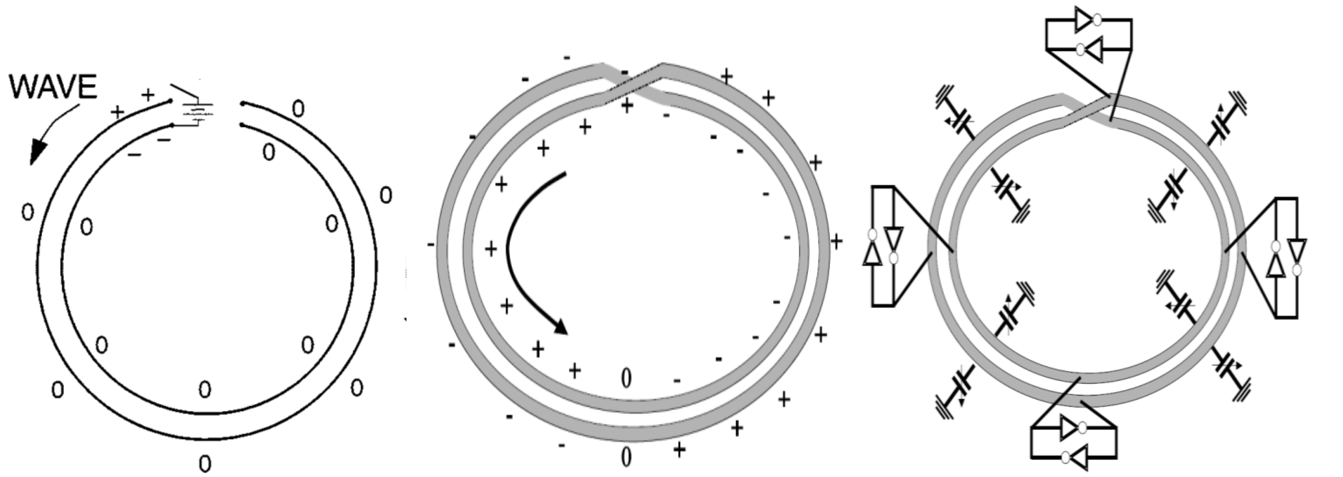

(a) Open loop ring (b) Möbius connected ring (c) Möbius inverter ring

Fig. 24: shows the oscillation based on the Möbius effect: (a) open loop differential ring, (b) Möbius connected differential ring, and (c) practical tunable Möbius connected differential oscillator circuit [37]]

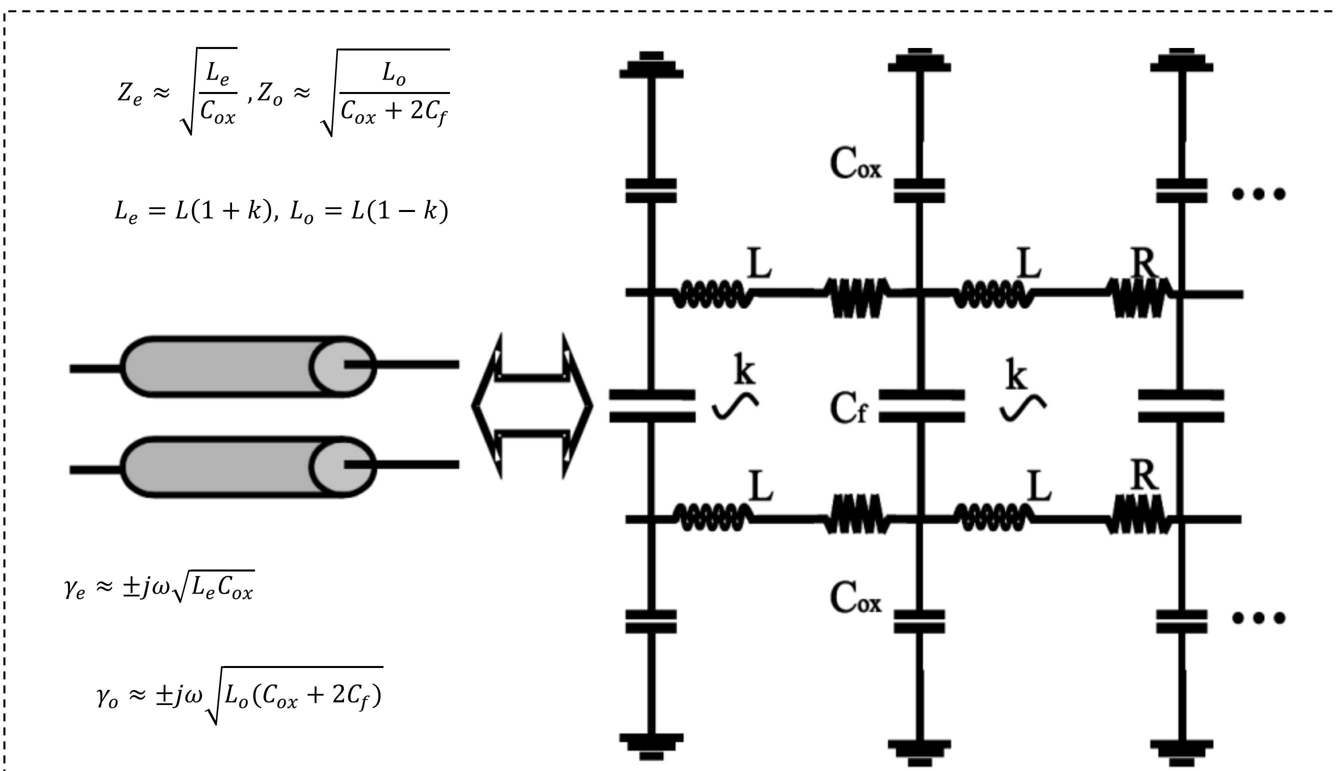

Fig. 25: Lumped representation of coupled-strip-line model (Z_e , Z_o are even and odd mode impedance, γ_e, γ_o are even and odd mode propagation constant, L_e, L_o are even and odd mode length) [36]

As shown in Figure (25), coupled line would support even and odd mode propagation. The even mode (fast wave mode) when the two lines are excited with the same signal, as a result, the coupling capacitance C_f between the two lines (Fig.25), will have no effect on the propagation constant 'γ'. The odd mode (slow wave mode), is obtained as the line pair is excited differentially, so the coupling capacitance between the two lines has a doubled effect on the propagation constant of this mode. For resonator application, slow wave propagation is of interest, care must be taken to suppress the even mode propagation.

Figure (26) shows the method of stable oscillation, inverters across the lines are providing gain and theoretically forcing the line to operate differentially, varactor diodes and centered ring provides even mode cancellation [35]-[37].

As shown in Figure (26) Möbius effect allows energy harvesting effects, energy is not lost at each stage but re-circulates in closed path). While the benefits of the Möbius connected wave-based oscillators are evident, this topology still limits the tuning range, limited to 10-20%. In this paper, a novel approach of improving the tuning range is suggested and validated with the practical example of 4-12 GHz/12-18 GHz oscillator based on Metamaterial-Möbius-strips resonator.

The phase-injections (perturbations) at different nodal points on strips improve the tuning-range and phase noise performance of Möbius strip based frequency-generating circuits. The oscillator circuit shown in Figure (27) works at DC bias of 5V and 35 mA, measured phase output power is typically 0dBm over the operating frequency band. The measured phase noise performance for 12-18 GHz VCO is -130dBc/Hz @ 1 MHz offset with 6000 MHz tuning, and phase noise performance is uniform within 3-5 dB variation over the operating frequency band.

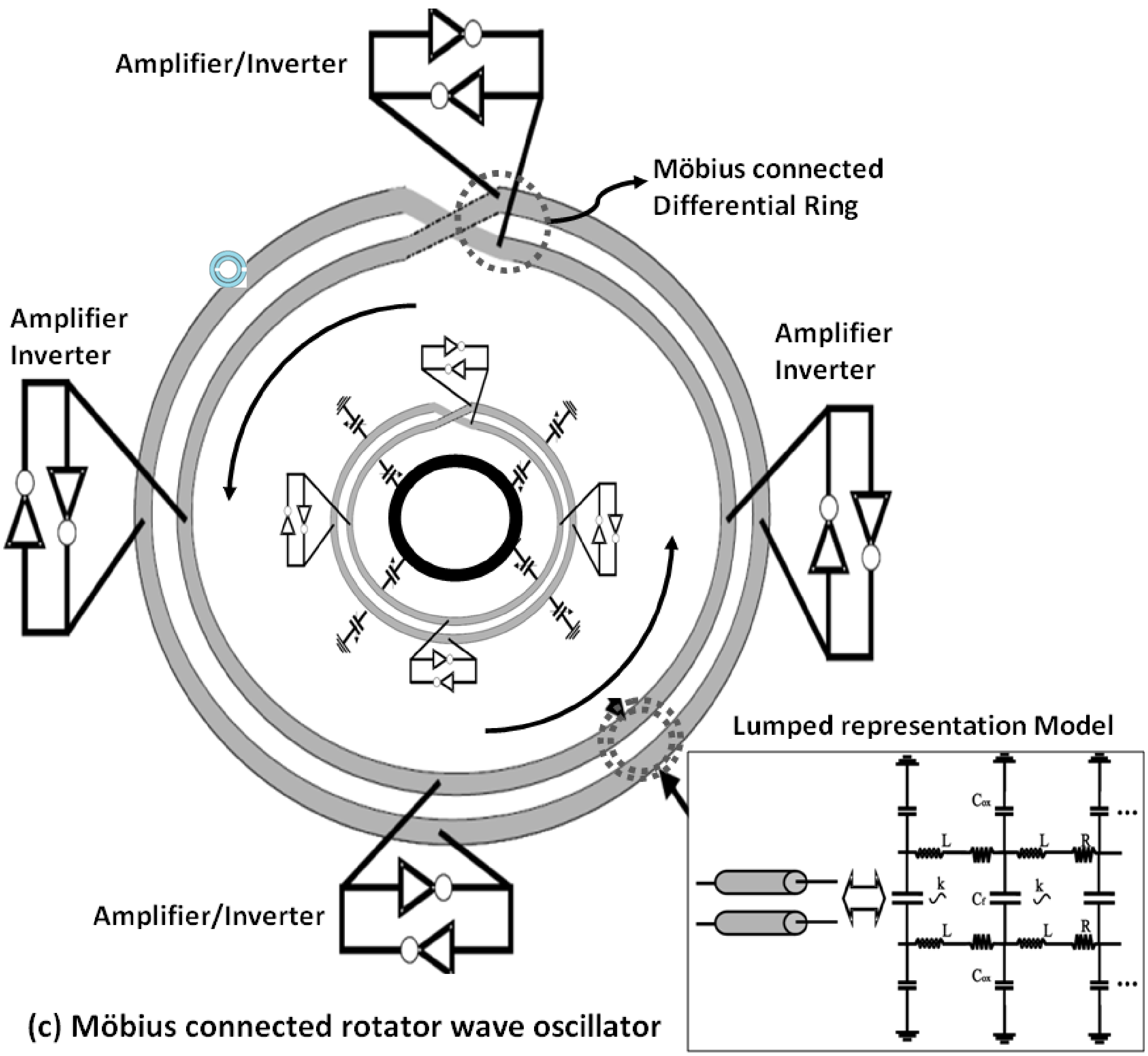

Fig. 26: Möbius connected rotary wave oscillator, distributed coupled lines composed of coupled lines equivalently represented as continuous limit of the multi-section lumped LC circuit)

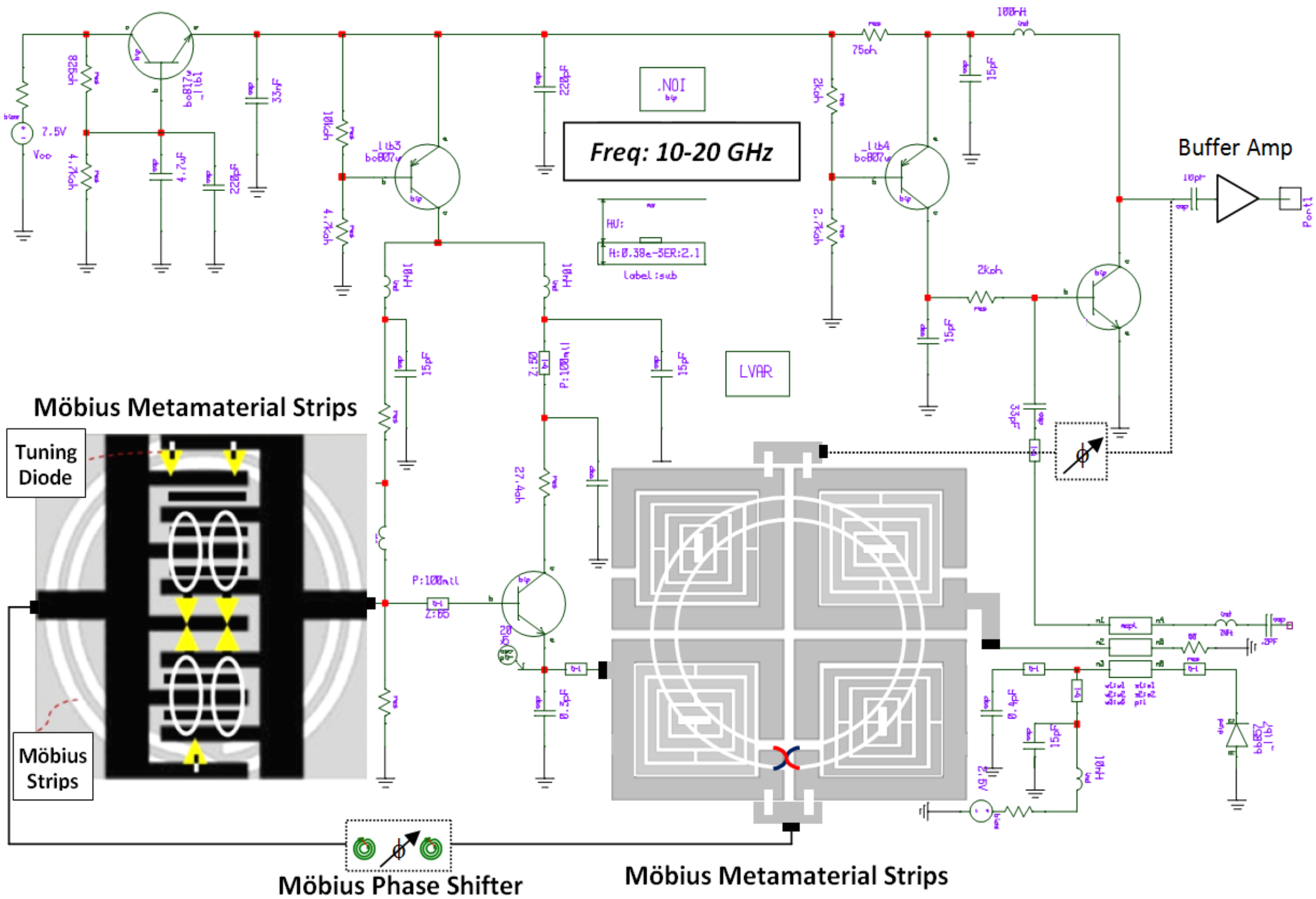

Fig.27: Layout of 12-18 GHz oscillator (0.75x0.75inches), using evanescent mode Metamaterial Möbius strips resonator network realized using 8 mils RT/Duroid 5880 with ε_r = 2.2

The novel NIMO (Negative Index Möbius Oscillator) circuit shown in Figures (28) is built on substrate (8-mill thick), uses BFP740 SiGeHBT transistor for providing negative resistance to compensate the losses of the resonator tank. The total DC power consumption is 680 mW that includes the buffer amplifier; operates at 8Volt and 85mA.

Figure (28) shows the typical schematic of 28.5GHz NIMO circuit that uses NIMS resonator as a tank network for improving evanescent mode coupled energy of the resonator tank module and coupled SRR for mode-locking and unwanted mode suppression. Figure (29) shows the measured phase noise plot is -144dBc/Hz @ 100 kHz offset with 10.56 dBm output power. The measured FOM (figure of merit) @ 1MHz is -226dBc/Hz for a given 680 mW DC power consumption. The main drawback of this configuration is limited tuning (<5%) to compensates the frequency drift due to change in temperature.

For practical applications, tuning range need to be improved. The tuning capability of NIMO circuit shown in Figure (28) is enhanced by incorporating phase-stabilization (manipulating the phase velocity by introducing Mode-Suppression Ring that allows multi-mode-phase-injection into the Mobius-Strips cavity), enabling Q-multiplier effect and exponential rise in Q-factor over the desired tuning range. Table 1 shows the recent published papers and compares this work based on FOM.

Table 1: Recent published oscillator’s performance and this work

References	f_o GHz	P_{DC} mW	P_o dBm	Tuning GHz	$L(f)$ dBc/Hz	FOM dBc/Hz
[38]	22.1	11.1	-11	20.6%	-109	-181
[39]	11.16	20	2.9	4.1%	-125.1	-193
[40]	12.4	30	7	2.5%	-122	-189.1
[41]	38.06	129.9	10.46	2.6%	-112.3	-182.7
[42]	28.33	15	0.3	-	-98.5	-176.4
This work Fig.28	**28.5**	**680**	**10.56**	**1.8%**	**-166.9**	**-226.7**

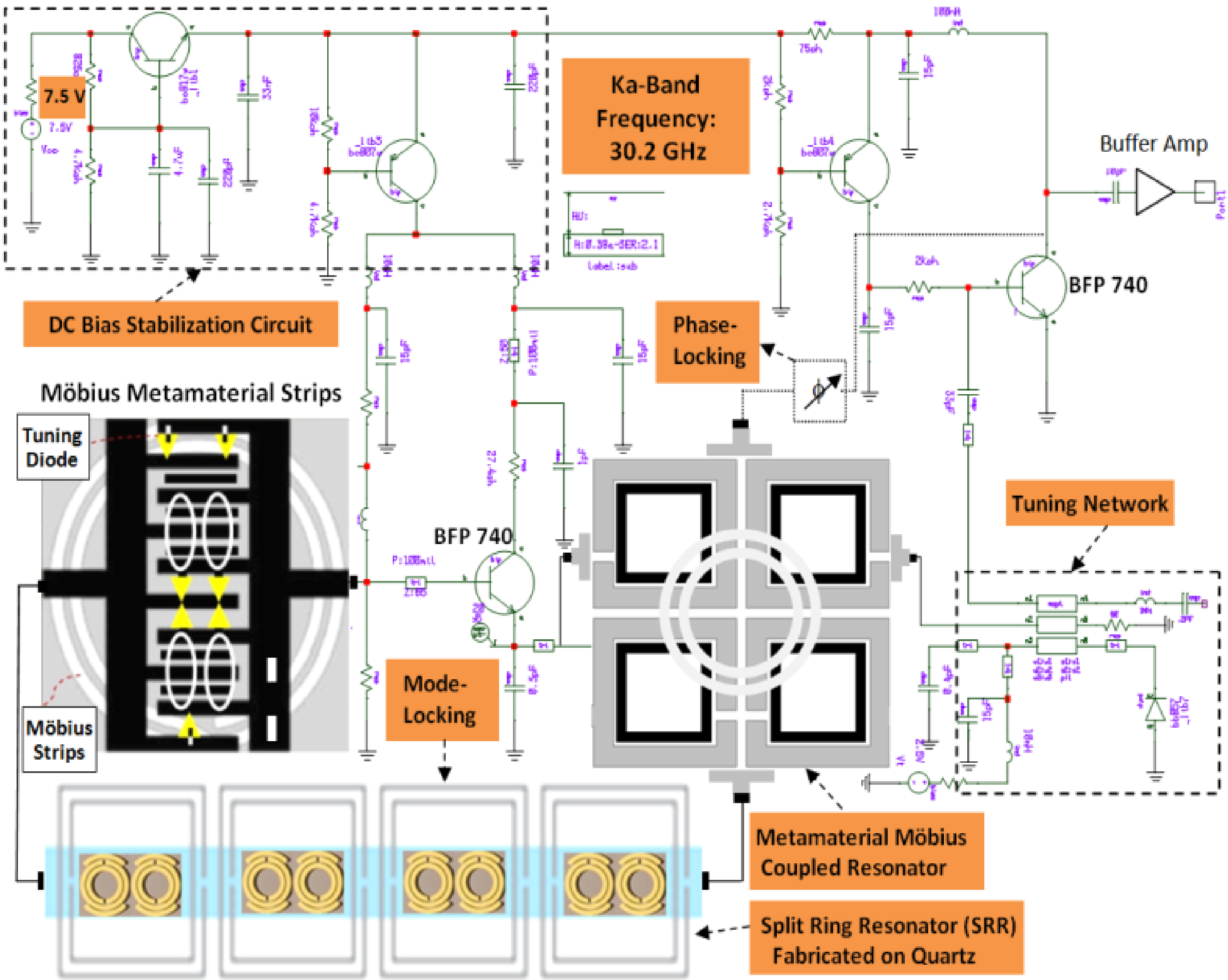

Fig.28: 28.5 GHz NIMO circuit ((ε_r =2.2, thick, 8-mil)

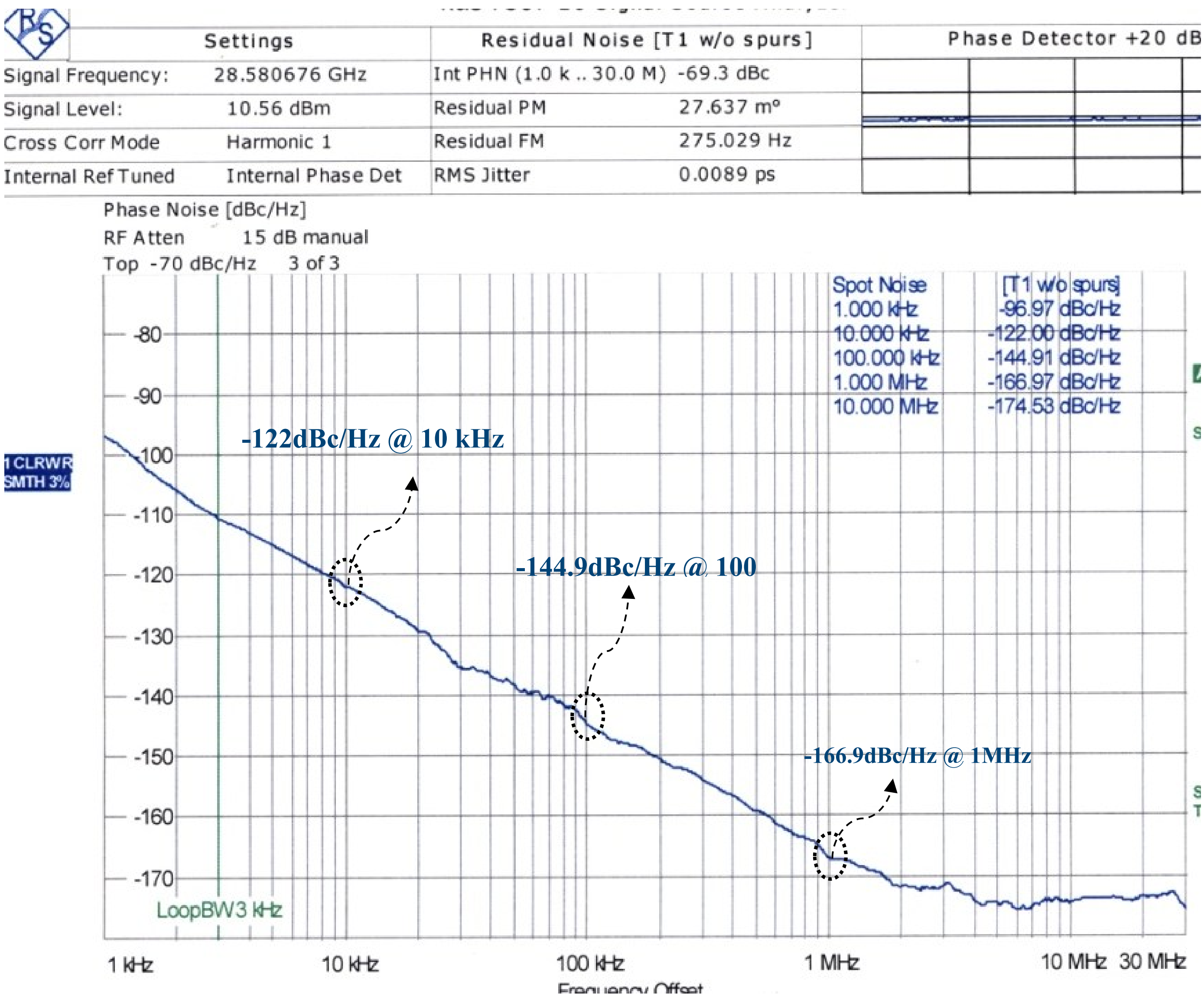

Fig. 29: Measured Phase Noise plot of 28.5 GHz NIMO (Fig. 28)

(b) Wireless and wearable electronics

Wireless and wearable implantable biomedical electronics are promising for continuous real-time measurement of underlying physiological signals such as electrocardiography in the heart [43], electromyography in the muscle [44], action potentials in brain [45] etc. In these biomedical devices, wireless power and data telemetry plays a key function that prolongs their operational life by promoting communication based on backscattering that can run without a battery or on single rechargeable battery.

Magneto-inductive telemetry is widely used in these devices for such wireless power and data transfer. The typical inductive telemetry core consists of a pair of antenna/coils placed coaxially in space, one inside the device and one placed externally as part of the reader/interrogator. The external coil typically transmits data which is also harvested for its power and regulated to power up the implant circuitry. The antennas used for such telemetry systems are either loop wire coils or printed spiral coils. One of the most important design criteria is to maximize the coupling coefficient between external and implanted coils, which affects the power/data transfer efficiency significantly.

Recently, there has been an effort utilizing metamaterial resonator for improved wireless energy transfer. Metamaterial resonators such as SRR can exhibit a strong magnetic resonance to EM wave [46], with high quality factor (Q) at resonance. This makes it an excellent candidate for near-field resonant power/data transfer. The SRR also enables sub-wavelength focusing of the incident energy at resonance in the capacitive gap of the Metamaterial which could be harvested for energy/power.
Compared to conventional antenna/coil system for power telemetry, SRR provides a compact and low profile geometry due to an integrated antenna and resonator function built into the structure [47].

Coupled Mode Theory (CMT) [48] predicts that when the resonances of both coils are matched, under the condition of the “strongly coupled regime”, it results in maximal energy transfer between coils. However, if the resonance of either of coils deviates from one another, the power transfer efficiency drops sharply. Since the biological environment is expected to vary due to physiological changes, it is very hard to match their resonances. This issue will be especially critical for any Metamaterial-based energy harvesters [49]-[50] due to their sharp narrowband resonance, thus automatic tuning of resonances will be necessary. This can be done for conventional coils with tunable varactors [51]-[52]. However the tuning needs precision and adds complexity in the system and moreover may be difficult with motion artifacts. The alternative approach is embedding of a non-foster impedance circuitry inside the SRR Metamaterial to achieve optimal power transfer over a broadband condition without the need for any tuning.

Current wireless power transfer (WPT) technology can only allow power transfer over a limited distance because, as the distance between the transmitter (Tx) and receiver (Rx) coils increases, the power transfer efficiency (PTE) decreases with a steep slope, while the electromagnetic field (EMF) leakage increases. In order to increase the PTE and decrease the EMF leakage simultaneously, we need to develop a method to concentrate the magnetic fields between the TX and Rx coils. In this paper, we proposed a novel Metamaterial structure to realize high efficiency and low EMF leakage. Metamaterial can confine the magnetic fields between the TX and Rx coils by negative relative permeability, including the reduction in leakage. Figure (30) shoes the typical arrangement of experimental setup for optimized efficiency of wireless power transfer [53].

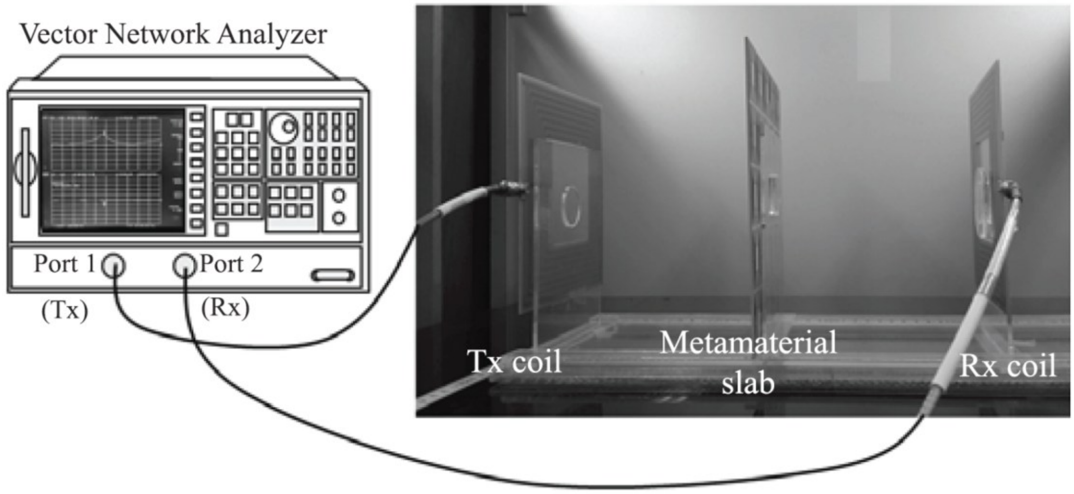

Figure 30: A typical experimental setup for the measurement of wireless power transfer efficiency [53].

(c) Artificial Gravitational Field

The generation of artificial gravitational fields with electric currents could be in principle detected through the induced change in space-time geometry that results in a purely classical deflexion of light by magnetic fields. Fuzfa [54] has proposed the experimental set-up shown in Figure (31) that includes stacked large superconducting Helmholtz coils for the generation of the artificial gravitational field and the detection would be achieved by highly sensitive Michelson interferometers whose arms contain Fabry-Perot cavities to store light into the generated gravitational field. As depicted in Figure (31), the amplitude of the phase shift accumulated during the bouncing of light in the curved space-time generated by the magnetic field would reach in a few months the level of an astrophysical source of gravitational wave passing through ground-based GW observatories [55]. Since space-time is slightly shrunk inside the superconducting coils coil, light trapped inside the powered coil accumulates phase shift as the round trips succeed each other. The sensitivity and dynamic range of superconducting coils can be increased by incorporating MMI (Möbius Metamaterial Inspired) superconducting coils. The ongoing research in MMI field could open new eras in experimental gravity and laboratory tests of space-time bends based on equivalence principle of general theory of relativity.

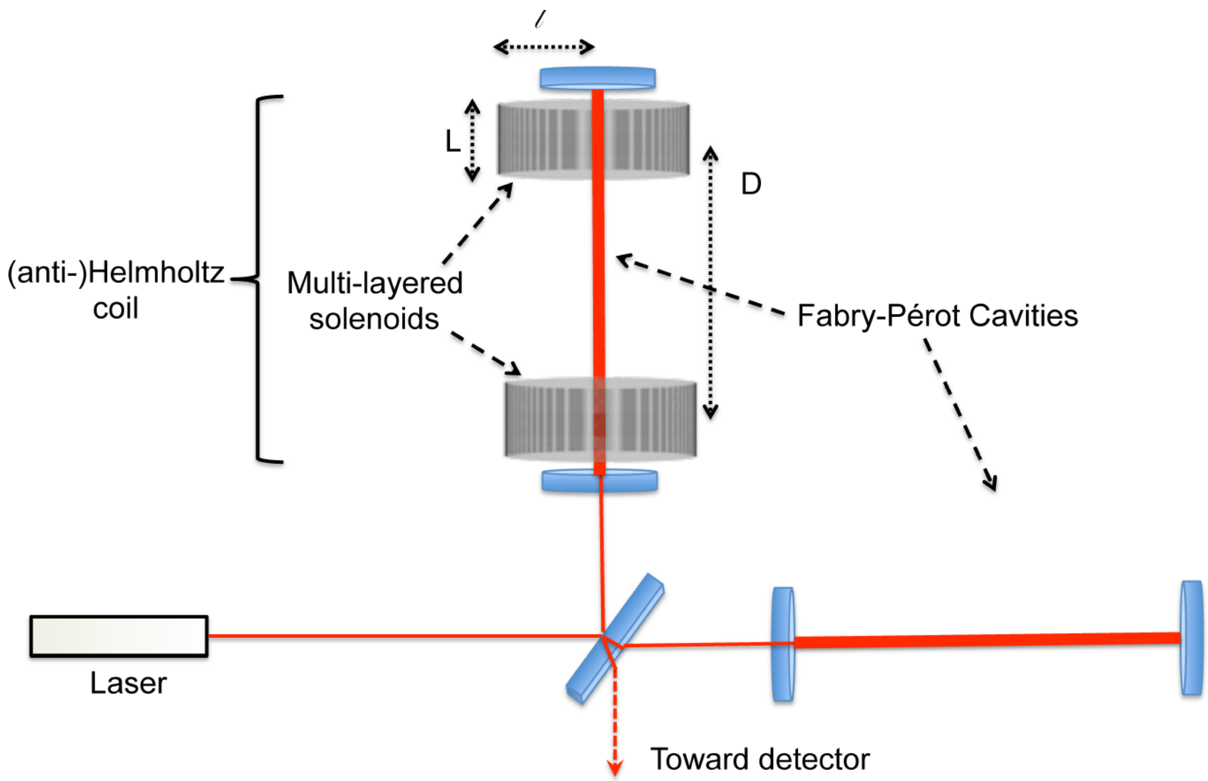

Figure 31: A typical schematic view of the experimental set-up for the measurement of gravitational wave [54]

Figure (32) illustrates the deflected trajectories of a bundle of rays incoming parallel light from spatial infinity, these trajectories have been obtained from the numerical resolution of geodesic equations in strongly curved space-times around loop of and solenoids with extremely large magneto-gravitational coupling (Cl) so that the way light is deflected can be easily shown. As shown in Figure (31), deflections of trajectories are plotted with different values of solenoid length (*L*), radius of current loop (*l*), and the magneto-gravitational coupling (Cl) strength [54].

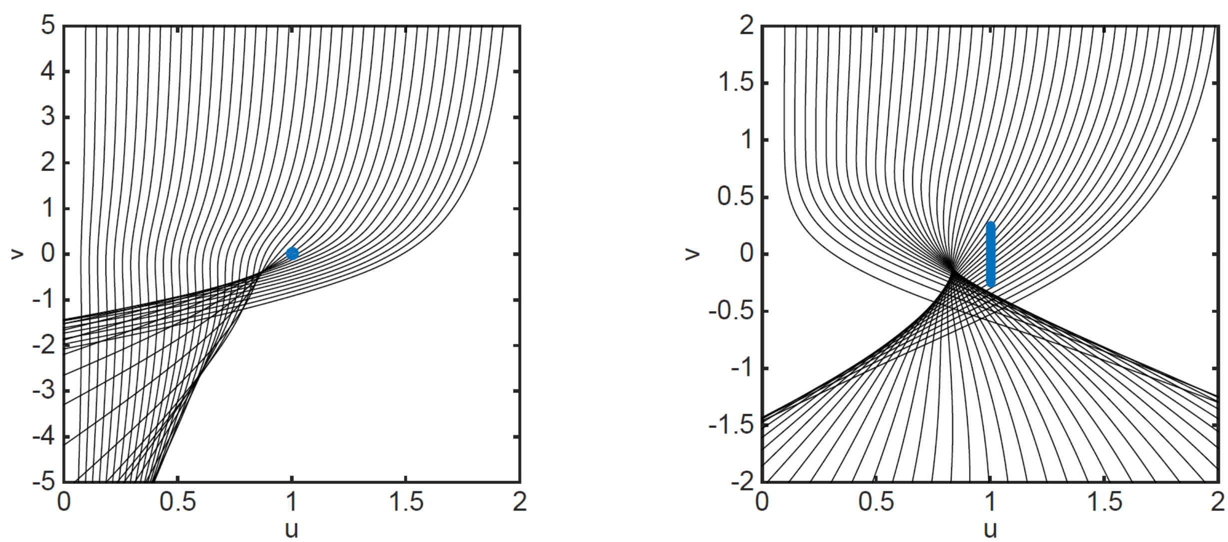

(a) C_l =10 and *L>>l* (b) C_l =10 and *L=0.5l*

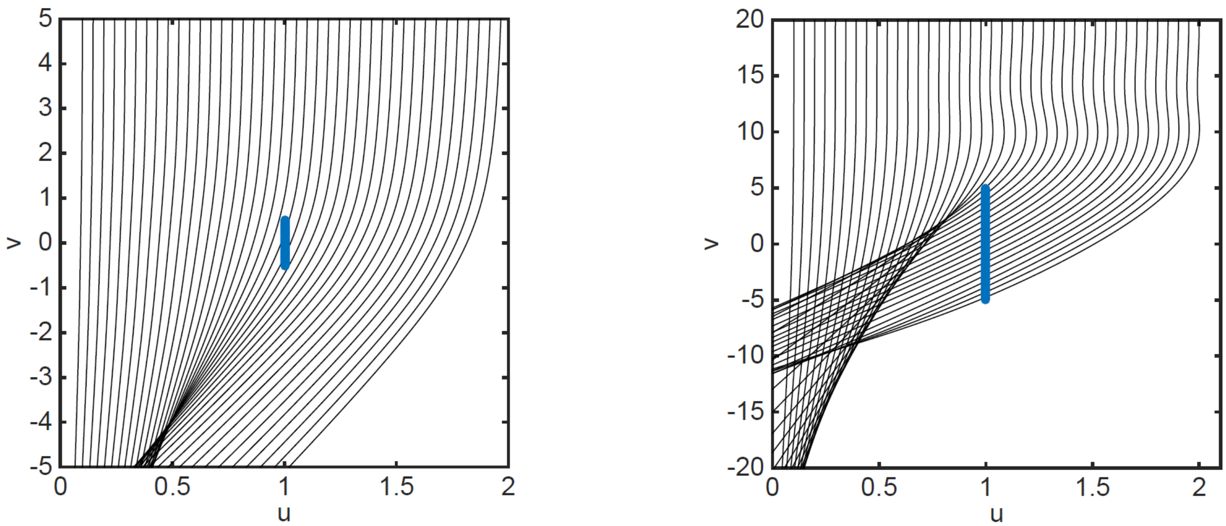

(c) *Cl* =10 and *L= l* (d) Cl =1 and *L=* 10*l*

Figure 32: shows the deflection of trajectories of parallel light rays coming from infinity [54]

MMI structures represent an artificial engineered material that can create and enable unique interactions of matter with electromagnetic and gravitational waves.

(d)MMI Superconducting Coils:

Superconductors offer unique advantages compared to ordinary metal, semiconductor and dielectric meta-atoms, namely: low loss, flux quantization and Josephson effects, quantum interactions between photons and discrete energy states in the meta-atom, and strong diamagnetism [56].

Figure (33) depicts the typical symbolic representation of a superconducting Metamaterial as a subset of meta-atoms and meta-molecules. As shown in Figure (33), superconducting quantum Metamaterial opens the possibility to explore collective quantum dynamics under very strong coupling between electromagnetic fields, gravitational field and artificial atoms [57].

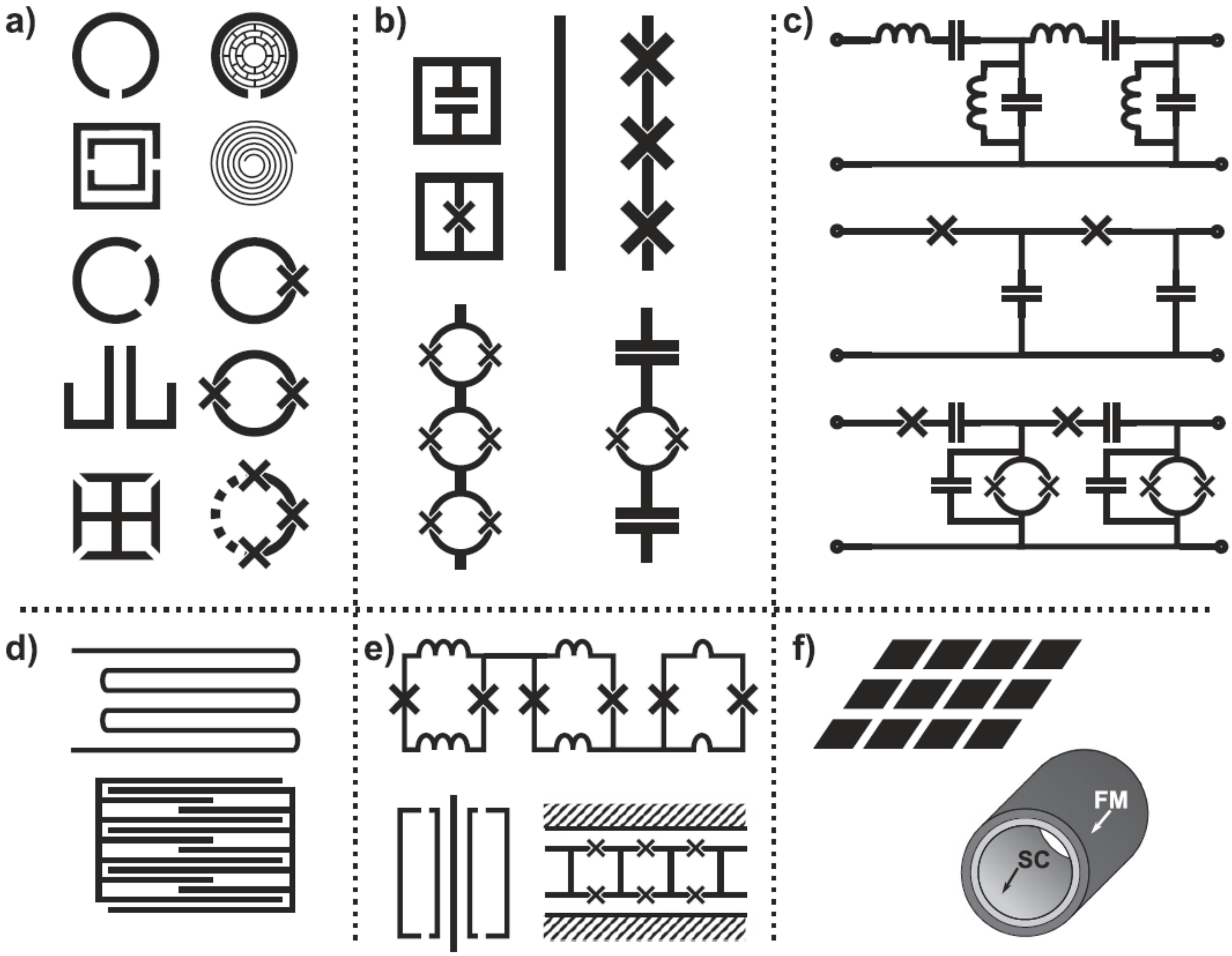

Figure 33: A typical symbolic representation of a superconducting Metamaterial as a subset of meta-atoms and meta-molecules: (a) Magnetically active meta-atoms, (b) electrically active meta-atoms, (c) transmission line Metamaterial, (d) lumped-element meta-atoms, (e) various meta-molecules realizations, and (f) dc magnetic cloak structures [57].

Metamaterial, where interaction strengths and length scales can be engineered, are a promising avenue for studying topological structure such as Möbius strips. Time-reversal broken topological Metamaterial have been realized in the microwave domain via a lattice of chiral magnetic (Gyrotropic) resonators [58]-[59]. Figure (34) shows the typical Möbius Metamaterial Insulator, realized by connecting the left and right edges of the system with a half twist and a spin flip (Fig 34b) [60].

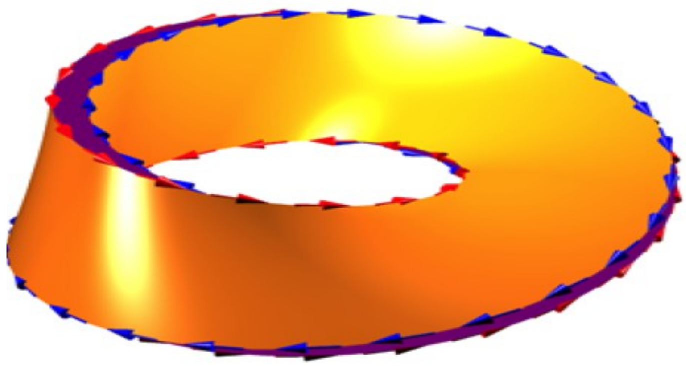

(a) Möbius TI, with the arrow indicating the edge propagation direction, and color the spin state

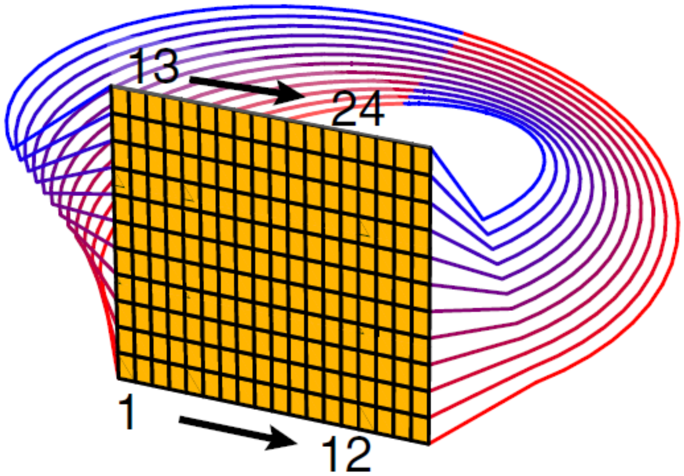

(b) Shows the connectivity of the Möbius TI, Metamaterial PCB is shown in orange, with external connections generating the topology indicating spin on traversing the edge

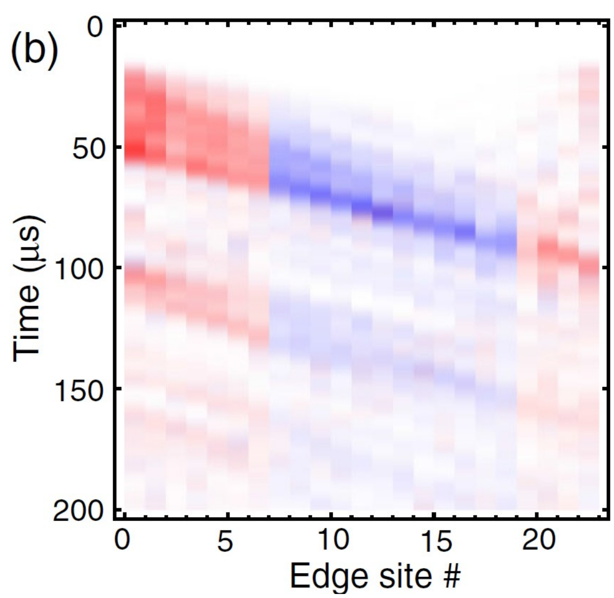

(c) Spin-resolved detection of edge transport after excitation of ↑; ↑ and ↓ intensities are plotted in the red and blue channels, respectively, showing the conversion from ↑ to ↓ when the excitation moves from one edge to the other, 3- round trips are visible.

Figure 34: shows the typical topological Möbius Metamaterial Insulator: (a) Möbius TI, (b) connectivity of the Mobius TI, and (c) Spin-resolved detection

As illustrated in Figure 34 (b), "a" inductor *j* sites from the top of the left edge is connected to the "b" inductor at the j sites from the bottom of the right edge. The spin flip is necessary, as "up" spins propagate rightwards on the top edge but leftwards on the bottom edge [61]. Figure 34(b) shows the temporal dynamics of a spin-up excitation in the system; it propagates rightward along the system edge, until it reaches the other edge, is converted into a down spin, and continues its progression around the system perimeter; this cycle is repeated until the excitation is damped out by the finite system Q.

V. Conclusion

This part discusses signals and sources with MMS resonator-based topology that enables next generation energy efficient signal source solutions in integrated circuit and surface mounted planar technology. The unique features of Möbius Metamaterial strip open to new inventions in the future, recurring in an endless– one could even say everything is going to be in the future in from of Möbius Strips Surface. More in . More in More in Opportunity, Emerging Trends, Challenges, and Future Directions.

REFERENCES

[1] Smith et al, "Determination of effective permittivity and permeability of Metamaterials from reflection and transmission coefficients," *Phys.Rev. B*, Vol. 65, No. 19, 195104, 2002

[2] Smith et al, "Electromagnetic parameter retrieval from inhomogeneous Metamaterials," Phys. Rev. E, Vol. 71, No. 3, 36617, 2005.

[3] U. C. Hasar and J. J. Barroso, " Retrieval approach for determination of forward and backward wave impedances of bianisotropic Metamaterials", PIER, Vol. 112, pp. 109-124, 2011

[4] Pendry et al, "Low frequency plasmons in thin-wire structures", *J. Phys.:Condens. Matter*, Vol. 10, No. 22, pp. 4785-4809, Jun. 1998.

[5] Marques et al, "Role of bianisotropic in negative permeability and left-handed metamaterials",Phys. Rev. B, Vol. 65, pp. 144440-1-6, 2002.

[6] Nicolson, A. M. and G. Ross, "Measurement of the intrinsic properties of materials by time-domain techniques", IEEE Trans. Instrum. Meas. Vol. 19, No. 4, 377-382, 1970.

[7] Weir, W. B., "Automatic measurement of complex dielectric constant and permeability at microwave frequencies," Proc. IEEE, Vol. 62, No. 1, 33-36, 1974.

[8] Milosevic eta al, "Effective Electromagnetic Parameters of Metamaterial Transmission Line Loaded With Asymmetric Unit Cells", IEEE Trans. on MTT, Vol. 61, No. 8, pp. 2761-2772, Au. 2013

[9] Landau et al " Electrodynamics of Continuous Media", 2nd ed. Oxford, U.K.: Pergamon, 1984.

[10] J. W. Graham, "Arbitrary oriented biaxial anisotropic media: wave behaviors and microstrip antennas", PhD Dissertation, Syracuse University, May 2012

[11] Koschny et al, "Impact of inherent periodic structure on effective medium description of left-handed and related Metamaterials," Phys .Rev. B, Condens. Matter vol. 71, Jun. 2005.

[12] A. Alù, "Restoring the physical meaning of metamaterial constitutive Parameters," Phys. Rev. B, Condens. Matter vol. 83, Feb. 2011

[13] Chen et al, "Determining the effective electromagnetic parameters of bianisotropic Metamaterials with periodic structures", PIERM, Vol. 29, pp. 79-93, 2013

[14] Chen et al, "Robust method to retrieve the constitutive effective parameters of Metamaterial', *Phys. Rev. E*, Vol. 70, No. 1, 16608, 2004.

[15] Ulrich L. Rohde, Ajay K. Poddar, " Möbius Metamaterial inspired next generation circuits and systems", Microwave Journal, May 2016

[16] Chen et al, "Retrieval of the effective constitutive parameters of bianisotropic Metamaterial", *Phys. Rev. E*, Vol. 71, 046610--9, 2005.

[17] Marques et al, "Metamaterial with Negative Parameters: Theory, Design and Microwave Applications, Wiley, 2008.
[18] Sydoruk et al, "Analytical formulation for the resonant frequency of split rings", *J. Appl. Phys.*, Vol. 105, No. 1, 14903, 2009.
[19] Chen et al, "Optimization approach to the retrieval of the constitutive parameters of a slab of general bianisotropic medium", PIERS, Vol. 60, 1-18, 2006.
[20] Li ET AL, "Determination of the effective constitutive parameters of bianisotropic Metamaterials from reflection and transmission coefficients," *Phys. Rev. E*, Vol. 79, 026610-1-7, 2009.
[21] Hasar, U. C., "Procedure for accurate and stable constitutive parameters extraction of materials at microwave frequencies, "PIERS, Vol. 109, 107-121, 2010.
[22] Wang ET AL, "A tunable left-handed metamaterial based on modified broadside-coupling split-ring resonators", PIERS Letters, Vol. 6, pp. 35–45, 2009
[23] Nakamura et al, "A 11.1-V Regulator-Stabilized 21.4-GHz VCO and a 11.5% Frequency-Range dynamic divider for K-Band wireless communication", MTT-Trans, vol.60, No. 9, pp. 2823-2832, Sept. 2012.
[24] Chen et al, "Design of high-Q tunable SIW resonator and its application to low phase noise VCO," *IEEE Microw. Wireless Compon. Lett*., vol. 23, no. 1, pp. 43–45, Jan. 2013.
[25] Collado et al, "Mechanically Tunable Substrate Integrated Waveguide (SIW) Cavity Based Oscillator", IEEE MWCL, vol. 23, no. 9, pp. 489–491, Sep. 2013.
[26] Chang et. al., "A new monolithic Ka-Band Filter-based voltage controlled oscillator using 0.15um GaAs PHEMT Technology", IEEE MWCL Letters, pp. 111-113, Vol. 24, No. 2, Feb 2014.
[27] Chen et.al., "Design of X-band and Ka-band Colpitts oscillators using a parasitic cancellation technique", IEEE Trans.Circuits System-I, Vol. 57, pp. 1817-1828, Aug 2010
[28] Ulrich L. Rode, Ajay K. Poddar, " Möbius Metamaterial inspired next generation circuits and systems", Microwave Journal, May 2016
[29] A. Poddar, "Slow wave resonator based tunable multi-band multi-mode injection-locked oscillator", Habil Thesis, BTU Cottbus, Germany, 2014
[30] S. A. Marvel et al, "Identical phase oscillators with global sinusoidal coupling evolve by Möbius group action", 2009 American Institute of Physics, pp. 043104-1- 043104-11, doi:10.1063/1.3247089
[31] E. Martens, "Cooperative behavior in networks of coupled oscillators", PhD Diss., Faculty of the Grad School of Cornell Univ. May 2009
[32] Rofougaran et al, "A 900 MHz CMOS *LC* oscillator with quadrature outputs," in *IEEE ISSCC Dig.Tech. Papers*, Feb. 1996, pp. 392–393
[33] Li Guansheng, E. Afshari, "A low phase noise multi-phase oscillator based on left-handed LC-Ring", JSSC. vol. 45, pp. 1822-1833, Sept 2010.
[34] Roman et al, "5-GHz oscillator array with reduced flicker up-conversion in 0.13-um CMOS", *JSSC*, vol. 41, no. 11, pp. 2457–2467, Nov. 2006.
[35] J. Wood et al., "Rotary travelling-wave oscillator arrays: a new clock technology," IEEE JSSC, vol. 36, no. 11, Nov. 2001.
[36] H.-T. Ahn , D. J. Allstot" A 0.5-8.5-GHz Fully Differential CMOS Distributed Amplifier", IEEE Journal of Solid State Circuits, vol.37, No.8, August 2002, pp. 985-993.
[37] D. Ham and W. Andress, "A circular standing wave oscillator", IEEE SSCC Dig. Tech. Papers, Feb. 2004
[38] Nakamura et al, "A 11.1-V Regulator-Stabilized 21.4-GHz VCO and a 11.5% Frequency-Range dynamic divider for K-Band wireless communication", MTT-Trans, vol.60, No. 9, pp. 2823-2832, Sept. 2012.
[39] Chen et al, "Design of high-Q tunable SIW resonator and its application to low phase noise VCO," *IEEE Microw. Wireless Compon. Lett*., vol. 23, no. 1, pp. 43–45, Jan. 2013.
[40] Collado et al, "Mechanically Tunable Substrate Integrated Waveguide (SIW) Cavity Based Oscillator", IEEE MWCL, vol. 23, no. 9, pp. 489–491, Sep. 2013.
[41] Chang et. al., "A new monolithic Ka-Band Filter-based voltage controlled oscillator using 0.15um GaAs PHEMT Technology", IEEE MWCL Letters, pp. 111-113, Vol. 24, No. 2, Feb 2014.
[42] Chen et.al., "Design of X-band and Ka-band Colpitts oscillators using a parasitic cancellation technique", IEEE Trans.Circuits System-I, Vol. 57, pp. 1817-1828, Aug 2010
[43] Riistama, J., et al. Sensors and Actuators A: Physical 157.2, 313 (2010).
[44] Young, Darrin J. "Wireless powering and data telemetry for biomedical implants." Engineering in International Conference of the IEEE 2009.
[45] Biederman, William, et al. Solid-State Circuits, IEEE Journal of 48.4, 960 (2013).
[46] Veselago, Victor Georgievich. Physics-Uspekhi 10.4, 509 (1968).
[47] Shelby, Richard A., David R. Smith, and Seldon Schultz, Science 292.5514, 77 (2001).
[48] Kurs, Andre, et al. Science 317.5834, 83 (2007).

[49] Hawkes, Allen M., Alexander R. Katko, and Steven A. Cummer. Applied Physics Letters 103.16, 163901 (2013).

[50Ramahi, Omar M., et al. Applied Physics Letters 101.17, 173903 (2012).

[51] Wilson, John M., et al. "Design of rotating MEMS tunable capacitors for use at RF and microwave frequencies." International Symposium on Microelectronics and MEMS. International Society for Optics and Photonics, 2001

[52] Poon, Ada SY, and Mazhareddin Taghivand. Proceedings of the IEEE100.7, 2207 (2012): 2207.

[53]Cho et al, "Thin PCB-Type Metamaterial for Improved Efficiency and Reduced EMF Leakage in Wireless Power Transfer Systems", IEEE Trans. on MTT, Vol. 64, No. 2, Fen 2016

[54] A. Fuzfa, "How current loops and solenoids curve space-time", Physical Review D; 13 December 2015; arxiv.org/abs/1504.00333

[55] W. Chaibi, R. Geiger, B. Canuel, A. Bertoldi, A. Landragin, P. Bouyer, " Low Frequency Gravitational Wave Detection With Ground Based Atom Interferometer Arrays", Jan 2016; http://arxiv.org/pdf/1601.00417v1.pdf

[56] Anlage S. M., "The physics and applications of superconducting Metamaterials", J. Opt-UK 13 024001

[57] P. Jung, A. V. Ustinov, and S. M. Anlage, "Progress in Superconducting Metamaterials", Superconductor Science Technology 27 (2014) 073001, doi:10.1088/0953-2048/27/7/073001

[58] Z. Wang, Y. D. Chong, J. D. Joannopoulos, and M. Soljačić, Reflection-Free One-Way Edge Modes in a Gyromagnetic Photonic Crystal, Phys. Rev. Lett. 100, 013905 (2008).

[59] Z. Wang, Y. Chong, J. D. Joannopoulos, and M. Soljacic, Observation of unidirectional backscattering-immune topological electromagnetic states, Nature (London) 461, 772 (2009).

[60] Ningyuan et al, "Time- and Site-Resolved Dynamics in a Topological Circuit", American Physical Society, DOI: 10.1103/PhysRevX.5.021031

[61] *L.-T. Huang and D.-H. Lee, Topological insulators on a Mobius strip, Phys. Rev. B 84, 193106*